1-26-2018

A Comparison of Small- And Medium-Scale Gravity Wave Interactions in the Linear and Nonlinear Limits

C. J. Heale
Embry-Riddle Aeronautical University, HEALEC@erau.edu

J. B. Snively
Embry-Riddle Aeronautical University, snivelyj@erau.edu

Scholarly Commons Citation

Heale, C. J., & Snively, J. B. (2018). A comparison of small- and medium-scale gravity wave interactions in the linear and nonlinear limits. Journal of Geophysical Research: Atmospheres, 123, 2454–2474. https://doi.org/10.1002/2017JD027590

AGU PUBLICATIONS

JGR

Journal of Geophysical Research: Atmospheres

RESEARCH ARTICLE
10.1002/2017JD027590

A Comparison of Small- and Medium-Scale Gravity Wave Interactions in the Linear and Nonlinear Limits

C. J. Heale[1] and J. B. Snively[1]

[1] Center for Space and Atmospheric Research (CSAR) and the Department of Physical Sciences, Embry-Riddle Aeronautical University, Daytona Beach, FL, USA

Key Points:
- The full nonlinear interactions induce small-scale wave breaking preferentially aligned with the phases of a medium-scale wave
- Linear assumptions do not accurately represent the distribution of momentum flux resulting from a small- and medium-scale wave interaction
- Time dependence and horizontal variations in medium-scale waves need to be included in GCM parameterizations to make them more accurate

Correspondence to:
C. J. Heale,
healec@erau.edu

Citation:
Heale, C. J., & Snively, J. B. (2018). A comparison of small- and medium-scale gravity wave interactions in the linear and nonlinear limits. *Journal of Geophysical Research: Atmospheres*, *123*, 2454–2474. https://doi.org/10.1002/2017JD027590

Received 14 AUG 2017
Accepted 19 JAN 2018
Accepted article online 26 JAN 2018
Published online 6 MAR 2018

Abstract A 2-D numerical model is used to compare interactions between small-scale (SS) (25 km horizontal wavelength, 10 min period) and medium-scale (MS, 250 km horizontal wavelength, 90 min period) gravity waves (GWs) in the Mesosphere and Lower Thermosphere within three different limits. First, the MS wave is specified as a static, horizontally homogeneous ambient atmospheric feature; second, a linear interaction is investigated between excited, time-dependent SS and MS waves, and third, a fully nonlinear interaction at finite amplitudes is considered. It is found that the finite-amplitude wave interactions can cause SS wave breaking aligned with the phase fronts of the MS waves, which induces a permanent mean flow and shear that is periodic in altitude. This impedes SS wave propagation into in the upper thermosphere and dissipation by molecular diffusion, when compared to linear amplitude simulations. Linear cases also omit self-acceleration-related instabilities of the SS wave and secondary wave generation, which modulate the MS wavefield. Neither the linear or nonlinear cases resemble the static approximation, which, by reducing a dynamic wave interaction to a static representation that is vertically varying, produces variable momentum flux distributions that depend strongly upon the amplitude and phase of the larger-scale wave. This is an approximation made by GW parameterization schemes, and results suggest that including time-dependent effects and feedback mechanisms for interactions between resolved and parameterized waves will be an important area for future investigations especially as general circulation models begin to resolve MS GWs explicitly.

1. Introduction

Gravity waves are ubiquitous in the Earth's atmosphere and can transport energy and momentum from tropospheric sources to the upper atmosphere (Fritts & Dunkerton, 1985; Hocke & Tsuda, 2001; Holton, 1982; Hung & Kuo, 1978; Kelley, 1997; Lindzen, 1981; Vincent & Reid, 1983; Yiğit & Medvedev, 2015). It is estimated that up to 70% of the momentum flux in the Mesosphere and Lower Thermosphere (MLT) region is due to gravity wave (GW) activity (Fritts & Alexander, 2003, and references therein). The deposition of this energy and momentum in the atmosphere has been shown to have important effects on the general circulation, such as the cold winter mesopause and the Quasi-Biennial Oscillation (e.g., Fritts & Alexander, 2003; Garcia & Boville, 1994; Nastrom & Fritts, 1992). Despite this, general circulation models (GCMs) can only resolve certain scales of waves in the atmosphere, and those scales that are unresolved require parameterization schemes (e.g., Lindzen, 1981; Matsuno, 1982; Meyer, 1999; Yiğit et al., 2008, 2009). Many parameterization schemes are limited in the physics that they capture, neglecting important effects such as transience, nonlinear effects, and secondary wave generation, while considering propagation through steady backgrounds only that are constrained to single vertical columns (Chen et al., 2005; Eckermann, 1997; Fritts et al., 2009; Hasha et al., 2008; Kim et al., 2003; Ribstein et al., 2015; Senf & Achatz, 2011). It has been suggested, however, that it is these unresolved small-scale (SS) waves (10–100 km wavelengths, minute-hour periods) that carry the largest momentum flux and could make the largest contribution to the energy and momentum budget in the MLT (e.g., Fritts et al., 2014).

It is important to note that there is a large variation in the physics and assumptions included in each GCM parameterization schemes. While early parameterization schemes assumed that waves deposited all of their momentum and energy once the Lindzen (1981) criteria are met (Alexander & Dunkerton, 1999; Holton, 1982), later schemes allowed for more realistic representations of dissipation by extending the breaking to multiple levels and including viscous dissipation in the thermosphere (e.g., Garcia et al., 2007; Matsuno, 1982; Meyer, 1999; Warner & McIntyre, 2001; Yiğit et al., 2008). Other GCM parameterizations used the Hines (1997)

Doppler spread parameterization framework (e.g., Akmaev, 2001; Fomichev et al., 2002; Schmidt et al., 2006); however, the validity of the Doppler spread theory has been questioned by several authors (e.g., Eckermann, 1997), and waves are typically damped exponentially to zero above 105 km. More advanced parameterizations schemes have included more sophisticated dissipation mechanism including ion friction, Newtonian cooling, and nonlinear interactions (Yigit & Medvedev, 2010; Yiğit et al., 2008) and have tried to include intermittency effects (de la Cámara et al., 2014). However, despite these advances, the majority of parameterization schemes uses single column approximations (i.e., they do not include horizontal propagation) and do not consider transience and time dependence of the GW fields nor the interactions between parameterized waves and resolved dynamics. Therefore, they cannot accurately capture the wave-mean flow interaction, distribution of momentum, and energy flux and thus exclude important nonlinear interaction effects such as resulting from self-acceleration and secondary wave generation. A description of the scope and limitations of parameterization schemes can be found in Kim et al. (2003), Alexander et al. (2010), and Yiğit and Medvedev (2016).

Recent papers have combined ray tracing with parameterization physics to attempt to overcome these limitations in application to wave/tidal interactions (e.g., Ribstein et al., 2015; Senf & Achatz, 2011). They find that the single column approach leads to significantly overestimated GW fluxes and underestimated solar tide amplitudes. Bölöni et al. (2016) used a ray tracing approach to investigate the relevance of GW-mean flow interactions and turbulent wave breakdown in contributing to GW drag, and how well Wentzel, Kramers, and Brillouin (WKB) theory captures these effects when compared to large eddy simulations. They found that the absence of transience effects in typical GW parameterizations leads to an oversimplified mean flow and advocated for the use of WKB-based ray tracing schemes in future parameterizations. However, as described in Yiğit and Medvedev (2016), WKB approximations require that vertical wave scales be smaller than vertical variations in the background field and that this limitation becomes restrictive in the thermosphere. Song and Chun (2008) and Amemiya and Sato (2016) developed ray tracing-based parameterizations that were implemented within a GCM for convective and orographic waves, respectively. While Song and Chun (2008) included time dependence explicitly, they only considered GW forcing by dissipation and not wave refraction. Amemiya and Sato (2016) considered forcing by dissipation and refraction but omitted explicit time dependence in favor of computational cost. Both found significant departures in the GW drag distribution from the column-based approach typically used in operational GCMs.

SS waves are subject to refraction by the background ambient atmosphere and other waves of different scales and periods. Depending on the background conditions, SS waves can be reflected, dissipated, or filtered leading to different distributions and dispersion of the wave, and ultimately determining where and when it will deposit its energy and momentum (Dunkerton & Fritts, 1984; Fritts, 1984; Fritts & Lund, 2011; Fritts et al., 1996, 2006; Heale, Snively, Hickey, et al., 2014; Hickey & Cole, 1988; Holton, 1982, 1983; Lindzen, 1981; Pitteway & Hines, 1963; Vadas, 2007; Vadas & Fritts, 2006; Vadas & Liu, 2009; Waterscheid & Hickey, 2011; Yiğit & Medvedev, 2009; Yiğit et al., 2008, 2009, 2012). For waves propagating in a vertically varying atmosphere, dissipation will typically occur in one of three ways. First, if the background wind becomes equal to the horizontal phase speed of the wave at some altitude, then the wave will encounter a critical level and will be absorbed into the background flow (e.g., Booker & Bretherton, 1967; Dunkerton & Fritts, 1984; Fritts, 1984; Fritts & Lund, 2011; Fritts et al., 2006; Holton, 1983; Lindzen, 1973; Yiğit & Medvedev, 2015). Second, a large-amplitude wave can become convectively and/or dynamically unstable and break (e.g., Achatz, 2007; Fritts, 1984; Lindzen, 1981; Yamada et al., 2001). Third, waves that do not have large enough amplitude to break will be dissipated by the molecular viscosity and thermal conductivity in the thermosphere (e.g., Heale, Snively, Hickey, et al., 2014; Heale, Snively, & Hickey, 2014; Liu, Xu, et al., 2013; Vadas & Fritts, 2005, 2006; Yiğit & Medvedev, 2015; Zhang & Yi, 2002). While propagation of SS waves through vertically varying background atmospheres has been extensively studied, the effect of a time dependently varying ambient atmosphere, which is horizontally inhomogeneous with respect to SS waves, has received less attention. It is likely that most of the temporal and horizontal variability on scales relevant to SS waves come from waves of larger scales. Indeed, recent advances in mesosphere airglow imaging capabilities and techniques have begun to uncover the complexity of the wave interactions and scales in the MLT region (Bossert et al., 2015; Fritts, Smith, et al., 2015; Heale et al., 2017; Moffat-Griffin et al., 2017; Yuan et al., 2016). Understanding the effects of these ambient waves on the propagation, dissipation, and filtering of high momentum flux SS waves is crucial to improving our knowledge of their effects on the atmosphere.

Numerical simulation and ray tracing have been used to study the interactions between waves of different scales in both the ocean and the atmosphere (e.g., Broutman & Young, 1986; Eckermann, 1997; Heale & Snively, 2015; Huang et al., 2014; Liu et al., 2008; Liu, Xu, Yue, et al., 2014; Sartelet, 2003; Senf & Achatz, 2011; Vanderhoff et al., 2008). These studies generally concluded that critical level filtering of waves propagating through a larger-scale wave/ambient wind field can be reduced significantly when time dependence of that larger-scale wave/ambient wind field is taken into account. This is because the location of critical levels change (or become non existent) as the amplitude and phase of the ambient wind/wave changes. In addition, from ray theory, the time-dependent background wind alters the ground-relative frequency of the SS wave in such a way that it tends to avoid the critical level (Huang et al., 2013; Lighthill, 1978). Heale and Snively (2015) also found a directional dependence upon the amount of SS wave energy that escapes reflection and critical level filtering. If the SS and medium-scale (MS) waves propagate in opposite horizontal directions, then critical and reflection levels become significantly less effective than if waves are propagating in the same horizontal direction. This is again due to the transient nature of the critical and reflection layers and the amount of time the SS wave spends "interacting" with these layers once time dependence is included.

As wave amplitudes increase, feedback can occur between waves and the mean flow. One such example is self-acceleration (Dosser & Sutherland, 2011; Fritts & Dunkerton, 1985; Fritts, Laughman, et al., 2015; Sutherland, 2001, 2006), in which a wave packet deposits its momentum into the background flow, which accelerates it to higher altitudes by altering its frequency. The lower fractions of the ascending packet experience this induced flow as a mean background wind/shear causing shifts to smaller vertical scales and often inducing breaking. It was found that this effect can cause breaking at a lower altitude, confined to a narrower altitude region, if wave-mean flow interactions are excluded (Liu, Xu, Liu, et al., 2014; Lund & Fritts, 2012). It was also found that this effect can occur more than once along a packet's propagation and at multiple altitudes (Fritts, Laughman, et al., 2015). While not described by linear theory, self-acceleration was incorporated into a GW drag parameterization by Scinocca and Sutherland (2010), suggesting that self-acceleration could be the reason why a central tuning parameter, the Froude number, has to be smaller than expected to fit observations. Wave breaking can also enhance the tidal amplitudes through the subsequent momentum deposition, but interactions are strongly dependent upon the phase of the tidal fields and GW (Liu et al., 2008; Liu, Lu, & Franke, 2013; Liu, Xu, Yue, et al., 2014; Yiğit & Medvedev, 2017). In ray tracing studies of GW and tidal interactions, the single column approach of most GW parameterizations schemes are shown to significantly overestimate GW fluxes in the MLT and underestimate tidal amplitudes (Lu et al., 2012; Ribstein et al., 2015; Senf & Achatz, 2011).

Other studies of nonlinear wave breaking and instability have cautioned that the usual assumptions of static and dynamic instability (i.e., Richardson number is smaller than 0.25 or less than 0) do not necessarily indicate when and where wave breaking can occur. Studies have been presented for cases of instability occurring both below and above the nominal instability criteria (e.g., Achatz, 2007; Fritts et al., 2006, 2009; Sonmor & Klaassen, 1997). It is found that instabilities at small amplitudes can arise as a result of wave interactions or superposition, while large-amplitude instabilities are finite amplitude versions of resonant interactions that can occur at small amplitude (Fritts et al., 2006; Sonmor & Klaassen, 1997).

In order to improve GW parameterizations, and ultimately GCM model predictions, developing a better understanding of the nonlinear mechanisms, feedback between waves of different scales and the mean flow, and departures from linear theory is of crucial importance. Despite significant progress by the studies cited in this introduction, the importance and extent of these mechanisms in the MLT are still not well understood. As stated in Liu (2016), addressing the increasing importance of small temporal and spatial scales is a challenge that requires the capture of complex interactions over a broad range of scales and altitudes. This is especially true as high-resolution GCMs begin to explicitly resolve the MS wave spectrum (e.g., Becker, 2009; Liu, McInerney, Santos, et al., 2014; Sato et al., 2012; Watanabe & Miyahara, 2009).

This study aims to investigate differences between SS and MS wave interactions in both the linear (small amplitude) and nonlinear (finite amplitude) limits, where the larger-scale wave is imposed as a static, horizontally homogeneous background (similar to assumptions made in most GCM parameterizations), as an analytically specified varying wave, or is specified as a fully dynamic propagating wave. The purpose of these investigations is to elucidate the importance of finite-amplitude interactions between these SS to MS waves. We use a 2-D, nonlinear, compressible numerical model to simulate the propagation, interaction, and energy

and momentum deposition of a typical SS wave (λ_x = 25 km, period = 10 min) in the presence of a typical (λ_x = 250 km, period=90 min) MS wave. We choose four scenarios to investigate.

1. Linear SS wave propagation through a static, horizontally homogenous,"background" MS wave, such that there is minimal interaction or energy exchange between the waves or the mean flow.
2. Linear SS wave propagation through a dynamic finite-amplitude MS wave, thus limiting interaction between the waves but allowing for more realistic energy exchange between the MS wave and the mean flow.
3. Finite-amplitude SS wave propagation through an analytically specified but dynamic background MS wave. Here the SS wave can evolve nonlinearly, but the MS wave behaves linearly and cannot exchange energy with the SS wave and mean flow.
4. Full interaction between finite-amplitude SS and MS waves and the mean flow at typical MLT amplitudes. We also assess the propagation of the SS and MS waves individually for comparison. This scenario is, indeed, most realistic.

The paper is organized as follows. Section 2 describes the numerical model and its initialization. Section 3 shows the results of individual SS and MS wave propagation. Sections 4–7 present the results from Cases 1–4 as listed above; finally, section 8 presents our summary and conclusions.

2. Numerical Model and Model Setup

2.1. Governing Equations

The numerical model solves the nonlinear, fully compressible, Navier-Stokes equations in 2-D using a finite volume method. The model is based upon the clawpack libraries (LeVeque & Berger, 2004) and is fully described in Snively and Pasko (2008), Snively (2013), and Zettergren and Snively (2015). The system of equations solved are

$$\frac{\partial \rho}{\partial t} + \nabla \cdot (\rho \mathbf{v}) = 0 \tag{1}$$

$$\frac{\partial}{\partial t}(\rho \mathbf{v}) + \nabla \cdot (\rho \mathbf{v}\mathbf{v} + p\mathbf{I}) = \rho \mathbf{g} + \nabla \cdot \boldsymbol{\tau} \tag{2}$$

$$\frac{\partial E}{\partial t} + \nabla \cdot \{(E + p)\mathbf{v}\} = \rho \mathbf{g} \cdot \mathbf{v} + (\nabla \cdot \boldsymbol{\tau}) \cdot \mathbf{v} + \kappa \nabla^2 T \tag{3}$$

$$E = \frac{p}{(\gamma - 1)} + \frac{1}{2}\rho(\mathbf{v} \cdot \mathbf{v}) \tag{4}$$

where ρ is density, p is pressure, $\mathbf{v}$ is the fluid velocity vector, m is the mass per particle, $\mathbf{I}$ is the identity tensor, $\mathbf{g}$ is gravity, T is the temperature, κ is the thermal conductivity, E is the total energy density, and γ is the ratio of specific heats (1.4 for our simulations). The viscous stress tensor is given by

$$\tau_{ij} = \mu \left(\frac{\partial v_i}{\partial x_j} + \frac{\partial v_j}{\partial x_i} - \frac{2}{3}\delta_{ij}\frac{\partial v_k}{\partial x_k} \right) \tag{5}$$

The main hyperbolic system of equation, along with the gravity term, is solved together using the f-wave method of Bale et al. (2002). The dissipation terms are solved separately using a time-split (fractional step) approach. For simplicity and control, the background ambient atmosphere is specified to be isothermal with a temperature of T = 240 K and is initially windless. The background ambient density is given by $\rho(z) = 1.2\exp(-z/H)$, where H = 7 km.

2.2. Wave Parameters and Numerical Domain

The SS wave is chosen to be consistent with waves typically observed in airglow studies and climatologies (e.g., Nielsen et al., 2009, 2012; Pautet et al., 2005; Suzuki et al., 2004; Taylor et al., 2009) and is specified to have a horizontal wavelength of 25 km, a period of 10 min, and initial vertical wavelength of 15.8 km. This gives the SS wave an initial horizontal and vertical phase speed of 42 m/s and −26.5 m/s, respectively, and an initial vertical group velocity of 18 m/s. For the finite-amplitude case, an initial temperature amplitude is chosen such that the wave achieves ∼5–10 K amplitude at the mesopause.

The MS wave parameters are chosen to be in accordance with those observed in Laser Imaging, Detection and Ranging (LIDAR) and Advanced Mesospheric Temperature Mapper (AMTM) data (Bossert et al., 2015; Fritts, Smith, et al., 2015; Fritts et al., 2014; Li et al., 2007; Lu et al., 2015, 2017; Suzuki et al., 2010; Yuan et al., 2016),

Table 1
Small- and Medium-Scale Wave Parameters Used in the Simulations

	λ_{x0} (km)	λ_{z0} (km)	Period (min)
Small scale	25	15.8	10
Medium scale	250	14.9	90

leading to a horizontal wavelength of 250 km, a vertical wavelength of 14.9 km, and a period of 90 min. The horizontal phase speed of this wave is 49.3 m/s, and the vertical phase and group velocities are −2.75 and 2.7 m/s, respectively. An initial temperature amplitude is chosen such that the wave reaches ∼10–15 K at the mesopause. The amplitude values for both waves are consistent with typically observed values in the MLT region. The small and medium-scale wave parameters are shown in Table 1.

The numerical domain is specified to be 500 km in the horizontal and 170 km in the vertical, with a resolution of 250 m in each direction and a model output every 60 s. The lower boundary is closed (reflective), the upper is open (waves can leave the simulation domain), and the sides are periodic. For simplicity, the horizontal domain size is equal to twice the horizontal wavelength of the MS wave; however, the SS wave is a localized packet. Both the SS and MS waves are excited using a time-dependent vertical body forcing in Cases 2 and 4 using the following form (note that the MS wave is specified as a "background atmosphere" in Cases 1 and 3):

$$F_z(x,z,t) = \rho(z)A \cdot \exp\left[-\frac{(z-z_0)^2}{2\sigma_z^2} - \frac{(x-x_0)^2}{2\sigma_x^2} - \frac{(t-t_0)^2}{2\sigma_t^2}\right] \cos[k(x-x_0) + m(z-z_0) - \omega(t-t_0)] \quad (6)$$

where $k = 2\pi/\lambda_x$, and $m = 2\pi/\lambda_z$.The parameters used in the vertical body forcing are shown in Table 2.

It is important to note that the model used in this study provides implicit large-eddy simulations, as it does not have the resolution, nor the third dimension, required to simulate the smallest scales of turbulence. The model does not require eddy viscosity nor explicit filtering, and features less than ∼10 grid points are damped by numerical viscosity. Therefore, the smallest scales we can accurately resolve are 2.5 km in wavelength. Since the model is 2-D, the case studies presented in this paper also represent interactions between waves that are aligned in azimuth. In reality, waves interact over a wide range of 3-D alignments, which can yield various results Thus, the interactions shown are most relevant to cases where horizontally extended (plane or frontal) sources generate a broad spectrum over a long period of time. In addition, 2-D breaking has been shown to overestimate the amplitudes of turbulent structures and can lead to longer decay times when compare to true 3-D breaking; however, we emphasize here the nonlinear interaction effects that occur over larger (wave and packet) scales instead (e.g., Fritts, Laughman, et al., 2015; Heale & Snively, 2015).

2.3. Case Studies

2.3.1. Individual Propagation of SS and MS Waves

The first cases will simulate the free propagation of the SS wave and MS wave, respectively, without the influence of the other. This gives a "benchmark" case to compare the interaction cases. The freely propagating MS wave simulation will also be used to define the static background "wave" for Case 1, by choosing a single vertical slice (at the middle of the domain), at two fixed times during the simulation. The momentum flux distributions and contributions to the mean flow for each of the waves will be examined.

2.3.2. Case 1

For typical GW parameterizations in GCMs, GWs are "launched" when certain conditions are met and a steady state solution is assumed at that time (i.e., no wave propagation time is considered). Any background waves present are represented by a static, horizontally homogeneous wind. As the next generation of high-resolution GCMs become operational, the MS GW spectrum can be resolved explicitly (e.g., Liu, 2016; Liu, McInerney, Santos, et al., 2014). These newly resolved waves will become an important part of the background atmosphere for the parameterized SS waves, and the limitation involved in omitting these interactions are important to consider. To approximate this case, a static, horizontally homogeneous, background atmosphere (defined from the MS simulation, as described above) is specified at two fixed times (to show how different the results can be depending upon the state of the background atmosphere when "frozen" in time).

Table 2
The Wave Forcing Parameters Used in the Simulation

	A (m/s)	z_0 (km)	σ_z (km)	x_0 (km)	σ_x (km)	t_0 (min)	σ_t (min)
Small scale	6.5×10^{-6}, 6.5×10^{-4}	10	3	100	25	5	10
Medium scale	0.06	80	15	0	∞	60	90

Note. The two amplitude values for the small-scale wave represent the linear and finite cases, respectively.

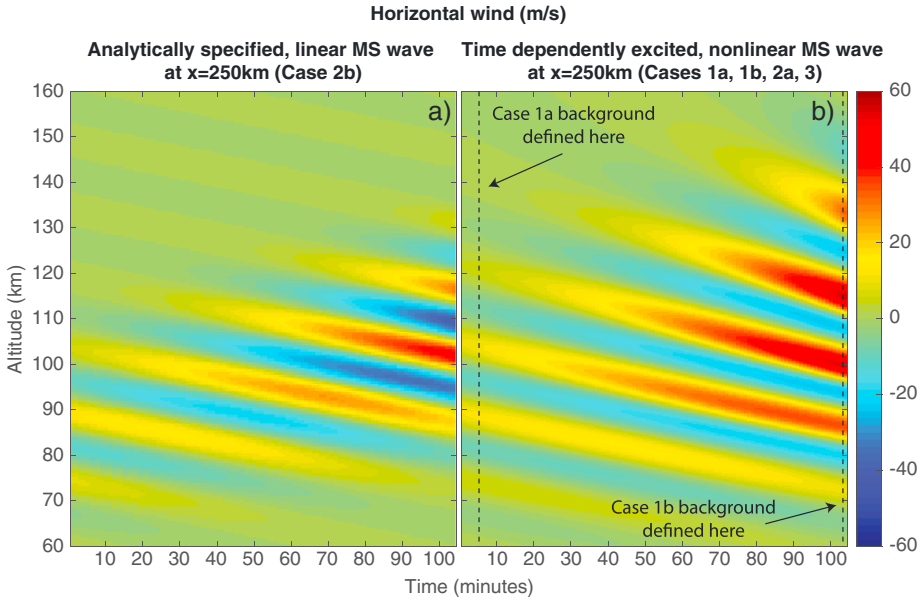

Figure 1. The evolution of the (a) analytically specified and (b) time dependently forced medium-scale (MS) wave at $x = 250$ km. The dotted lines represent the stationary profiles used for Cases 1a and 1b.

A linear amplitude SS wave will be excited and propagate through this background. One of the challenges in reducing an inherently dynamic process to a static representation is choosing the time at which to "freeze" the MS wave background. Since, in typical operational GCM parameterization schemes, the wave propagates from its source to dissipation region "instantly" as soon as it is generated, we will choose the point at which the SS wave is at peak excitation in the troposphere to freeze the MS wave (note that in reality the SS wave takes time to propagate up from its source region to the region where it dissipates, over which time the MS wave evolves). For comparison, we will choose another time (100 min later, the approximate time the SS wave would take to reach the thermosphere from the source region), when the MS wave has propagated further up into the atmosphere, evolved, and grown in amplitude (by a factor of ~3–4) as a result of decreasing density. This shows how much the MS wave evolves over the time considered to be "instant" in typical GCM parameterizations, and how different the influence is on the SS wave. The times at which these profiles are taken are shown by the dotted line in Figure 1.

2.3.3. Case 2

This case will represent the propagation of the SS wave in the linear limit, while the MS wave is fully specified, dynamic, and of finite amplitude. This will add a level of complexity to Case 1 but limit interactions between the SS and MS waves. The MS wave, however, grows large enough in amplitude to deposit into the mean flow as it propagates upward. The upward group propagation and associated amplitude growth are completely absent in the static background case. The MS wave evolves considerably over the course of the interaction with the SS wave. Thus, time dependence needs to be included to accurately capture the dynamics of the interaction. The parameters of the forcing are specified in Table 2, with the SS wave peak forcing amplitude of 6.5×10^{-6} m/s. The evolution of the MS wave (at $x = 250$ km) for this case is shown in Figure 1b.

2.3.4. Case 3

This case uses a time dependently forced, finite-amplitude SS wave (6.5×10^{-4} m/s) propagating through an analytically specified but dynamic MS wave. As a result of this, the MS wave includes the effects of group velocity and the increase in amplitude with altitude; however, it does not include dispersion, nonlinear effects, or dissipation (although dissipation of the MS is small over the duration of the simulation). There is also no energy exchange between the SS and MS waves, nor the MS wave and the mean flow. The evolution of the MS wave (at $x = 250$ km) for this case is shown in Figure 1a.

2.3.5. Case 4

This case considers the interaction between the SS and MS waves in the nonlinear limit, where both are at finite, realistic, amplitudes. This case allows for energy exchange and feedback between the two waves in addition to the ambient flow. As discussed in section 2.2, the peak temperature amplitudes at mesopause height reach ±5–10 K to be consistent with observational evidence; however, the amplitudes in the thermosphere

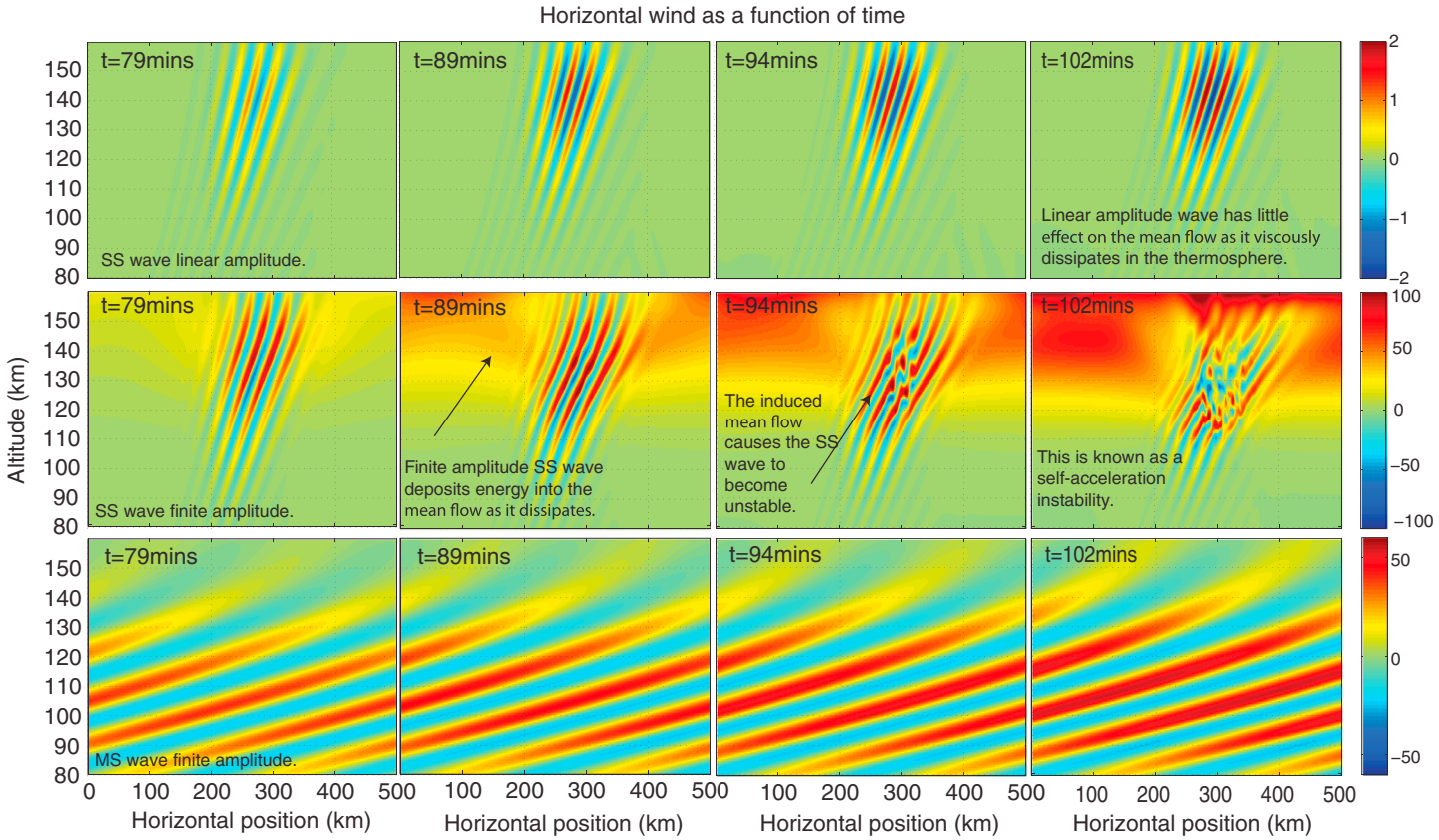

Figure 2. The time evolution of the linear small-scale (SS) wave, finite-amplitude SS wave, and finite-amplitude MS wave at t = 79, 89, 94, and 102 min.

are much larger (~ ±20 K). The peak forcing amplitude of the SS wave in the troposphere is 6.5×10^{-4} m/s as described in Table 2.

The degree of SS wave nonlinearity is controlled, in each of the four cases, by the choice of initial amplitude. For the MS wave, the inclusion/omission of nonlinear interactions with the SS wave and the mean flow is determined by whether the MS wave is explicitly excited within the model (included) or is specified as a background atmosphere (omitted).

2.3.6. Momentum Flux Analysis

For each of the cases, the time-averaged distribution of the SS wave's momentum flux will be examined. However, since the linear and finite-amplitude SS waves will have vastly different momentum flux amplitudes (peak forcing amplitudes differ by a factor of 100), the distributions are normalized to the peak value at the launch altitude (of each case) so that the relative momentum flux values can be compared between simulations. The equation is given by

$$MF_{\text{norm}} = \frac{\overline{u(z)'w(z)'}}{\max(u(z = 10\ \text{km})'w(z = 10\ \text{km})')} \tag{7}$$

where u' and w' represent the SS wave horizontal and vertical perturbation velocities, respectively, and the overbar represents a time average over the duration of the simulation.

3. Individual Propagation of SS and MS Waves

In this section, we present results of the SS and MS waves propagating individually, as a control to compare with the interaction case studies in the next section. Figure 2 shows a time sequence of the linear and finite-amplitude SS waves, and the MS wave showing their evolution.

While it is clear that the linear SS wave simply propagates upward as a packet and dissipates strongly above 155 km, the finite-amplitude SS case shows significant energy deposition into the background flow, leading to a strong induced flow at high altitudes (above 130 km altitude). This induced wind causes a refraction

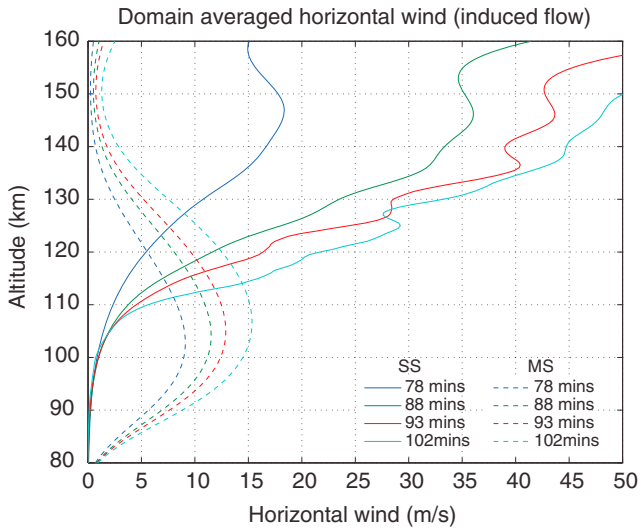

Figure 3. The domain averaged horizontal wind for the finite-amplitude small-scale wave (solid lines) and medium-scale wave (dotted lines) at $t = 79$, 89, 94, and 102 min.

of the SS wave to shorter vertical wavelength as time progresses; eventually, breaking occurs at $z = 135$ km. This is known as a self-acceleration instability and is the same effect as described by Lund and Fritts (2012), Liu, Xu, Liu, et al. (2014), and Fritts, Laughman, et al. (2015). The MS wave not only propagates upward and grows in amplitude without any dramatic effect but also deposits momentum in the background flow, inducing a positive (rightward) wind. It is also noted that the MS wave shows no visible signs of breaking despite its perturbation amplitude being greater than the horizontal phase speed of the wave.

The induced background flow can be seen in Figure 3, which shows the domain averaged horizontal wind (induced wind) at the same four times as Figure 2. We note that the localization of the SS wave packet should lead to a relatively localized induced wind also; therefore, the overall amplitude of the wind may be overestimated due to "wrap-around" effects of the periodic boundary conditions.

The MS wave induces an approximately Gaussian shaped flow that follows the packet as it propagates upward and grows in amplitude. By the end of the simulation at $t = 102$ min, the induced wind peaks at $z = 107$ km with an amplitude of 15 m/s. It is noted that this would continue to get stronger if the simulation were run for longer. The SS wave generates a flow at much higher altitudes with a peak (~18 m/s) developing at $z = 147$ km altitude at $t = 78$ min. This then develops into a wave-like structure by 93 min when breaking is present. The permanent induced flow and shear are responsible for the refraction of the packet to smaller vertical wavelengths and the eventual breaking. This induced breaking is consistent with the late stages of a self-acceleration instability (Dosser & Sutherland, 2011; Fritts, Laughman, et al., 2015; Lund & Fritts, 2012; Sutherland, 2006).

In order to quantify the momentum flux distribution in the linear and nonlinear cases, we take the time-averaged and normalized momentum flux (as described in equation (7)) and plot them in Figure 4. As previously mentioned, the linear amplitude wave will clearly have very small momentum flux values compared to the finite-amplitude case, so the normalization of the momentum flux values allows for comparisons of the relative differences in the momentum flux distributions.

The linear amplitude SS wave has a time-averaged, normalized momentum flux profile that is roughly packet shaped, with a maximum relative value of 3×10^{10} at 141 km. The finite-amplitude SS wave has a deeper (in altitude) momentum flux distribution. Its maximum relative value is approximately a factor of 10 smaller than the linear case and occurs lower ($z = 135$ km) the height at which breaking occurs. This same result was found in Lund and Fritts (2012), who found that breaking occurred at lower altitudes, and was much more

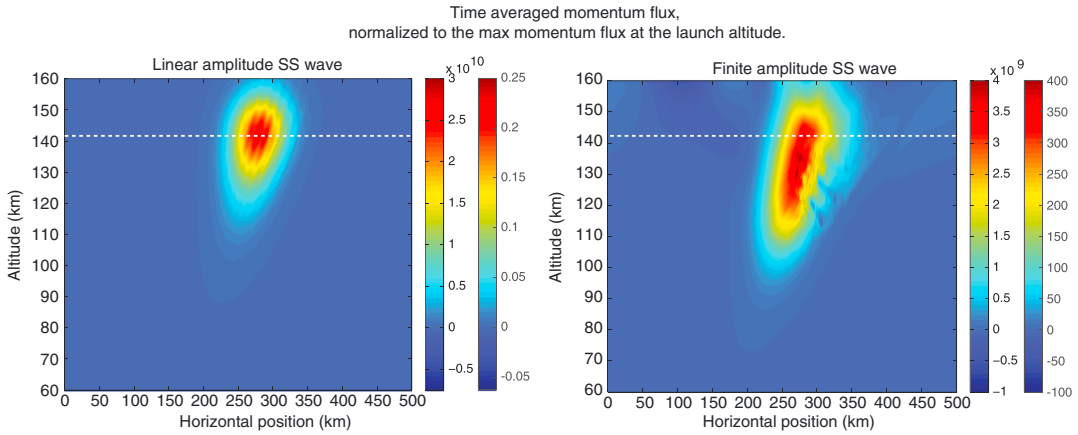

Figure 4. The time-averaged momentum flux, normalized to the maximum value at the launch altitude ($z = 10$ km), for the linear (left) and nonlinear (right) amplitude small-scale (SS) waves. The second color bar (on the outside) shows the scale for the absolute time-averaged momentum flux for comparison.

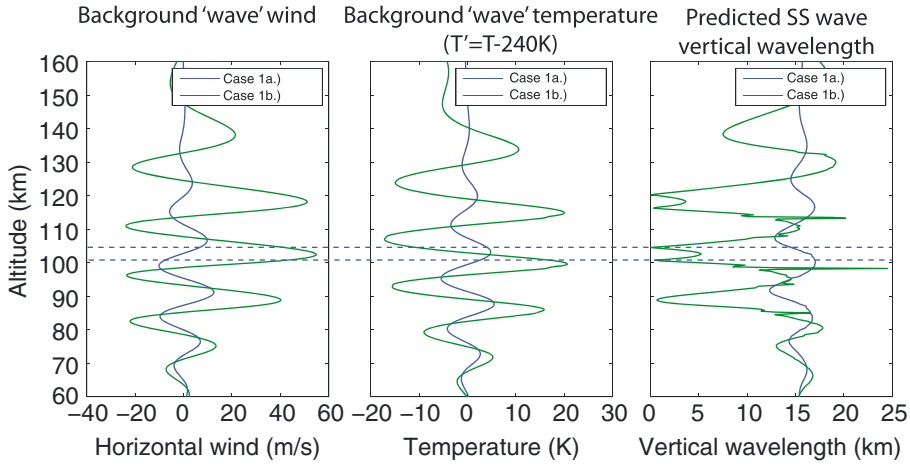

Figure 5. The background specified wind and temperature perturbation profiles for each of the two simulations, and the predicted small-scale (SS) vertical wavelength. The dotted black lines indicate critical levels in Case 1b.

confined in altitude, when the wave was allowed to influence the mean flow. The shape of the distribution is also asymmetric with the leading side of the packet being more disturbed than the trailing side. If the normalized momentum flux values in the one case are larger than another, it is an indication that more of the waves total momentum and energy wave have propagated higher and the packet has stayed more coherent. This is why the linear case has larger relative momentum flux values than the finite-amplitude case. The linear case does not lose momentum through breaking or strong mean flow deposition, and so it propagates and dissipates as a coherent packet in the thermosphere. The nonlinear case however breaks, undergoes self-acceleration, and nonlinearly deposits momentum into the background over a range of altitudes. Therefore, more of the wave momentum is lost lower down in the atmosphere and is distributed over a larger region, leading to smaller relative values. The absolute time-averaged momentum flux scale is also plotted in Figure 4 for comparison (outside scale).

4. Case 1: Linear SS Propagation Through a Static, Vertically Varying Background Specified Wave

As mentioned in section 2.3, the wave background was specified using a single vertical slice from the individually propagating MS wave simulation at two fixed times: Case 1a.) At the time the SS wave's source reaches its peak forcing in the troposphere ($t = 5$ min; representative of the GCM assumption that the background is stationary at the launch time of the parameterized GWs). Case 1b.) At the end of the simulation ($t = 102$ min), when the MS wave has propagated and increased in amplitude (because, in reality, the background would evolve over the time it takes the SS wave to propagate up to the MLT, and this is not captured in parameterizations). The two background profiles and predicted vertical wavelength for the SS wave propagating through those backgrounds are shown in Figure 5.

Figure 5 clearly shows how much the amplitude of the MS wave grows between the time the SS wave is launched (Case 1a) and the end of the simulation (Case 1b). Because of this, vastly different vertical wavelength profiles with altitude are predicted for the SS wave in each case. This shows the importance of considering the time dependence and evolution of the background medium-frequency waves over the course of the SS wave propagation, interaction, and momentum deposition processes. This will be an especially important consideration for high-resolution GCMs that resolve the MS wave spectrum.

Figure 6 shows a time sequence of the SS wave propagation in each of the simulations (note that the background wave has been subtracted to show only the SS waves). For Case 1a, there is minimal refraction of the SS wave by the background MS wave because its amplitudes are small (~10 m/s). The SS wave propagates upward and dissipates in the thermosphere with little filtering. The distribution of the time-averaged, normalized momentum flux shown in Figure 7 is almost identical to the SS wave propagating freely as in Figure 4,

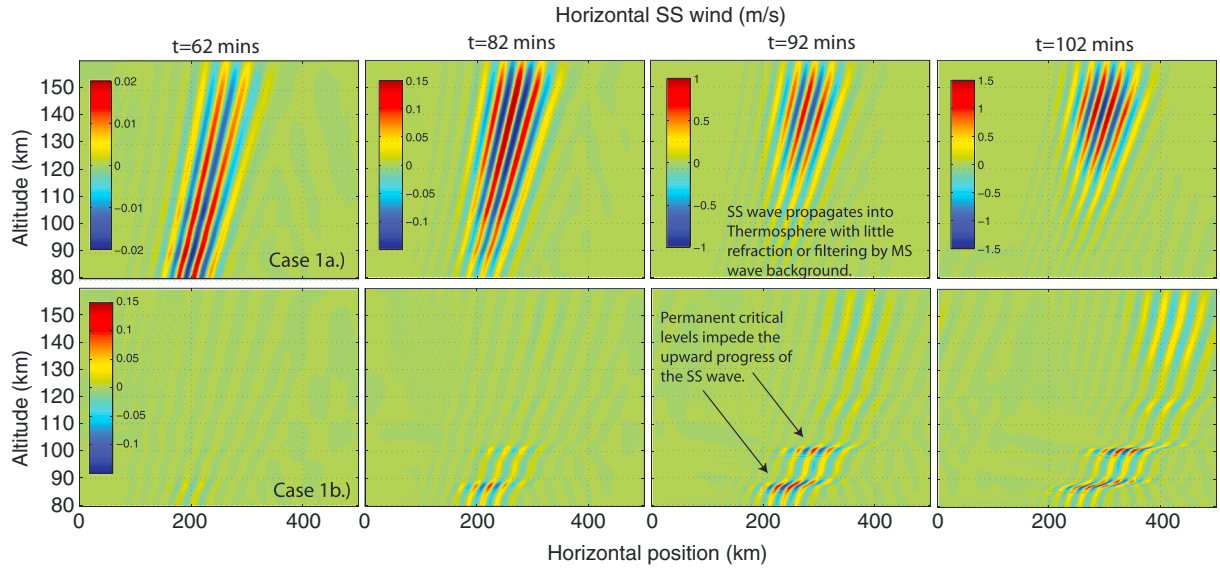

Figure 6. A time sequence of the SS wave propagation through the static, vertically varying background imposed MS waves (which are subtracted from figure for ease of interpretation). The Case 1a background is specified by a vertical slice of the MS wave at the time the SS wave is launched, while Case 1b is specified by a vertical slice of the MS wave taken at the end of the fully time dependent simulation.

except the relative peak amplitude is approximately 100 times less. For the Case 1b simulation, the SS wave shows strong filtering by the critical levels at 90 and 100 km as predicted in Figure 5. This severely hinders the propagation of the SS wave into the thermosphere as shown in the time-averaged, normalized momentum flux. The momentum flux is maximized near 85 and 100 km altitude but at peak magnitudes of 1,000 times less than for Case 1a. Also note that the momentum flux that reaches the thermosphere has a peak value that occurs at a higher altitude than in Case 1a. This is because the portion of the SS packet that avoids critical level filtering and reaches the thermosphere is that with the largest vertical scales and phase speeds that are able to propagate the highest.

Case 1 shows the limitations of reducing a dynamic interaction to a static, homogenous case, and highlights how different the SS wave propagation and momentum flux distribution can be depending upon the time at which the MS wave is essentially frozen as a background atmosphere.

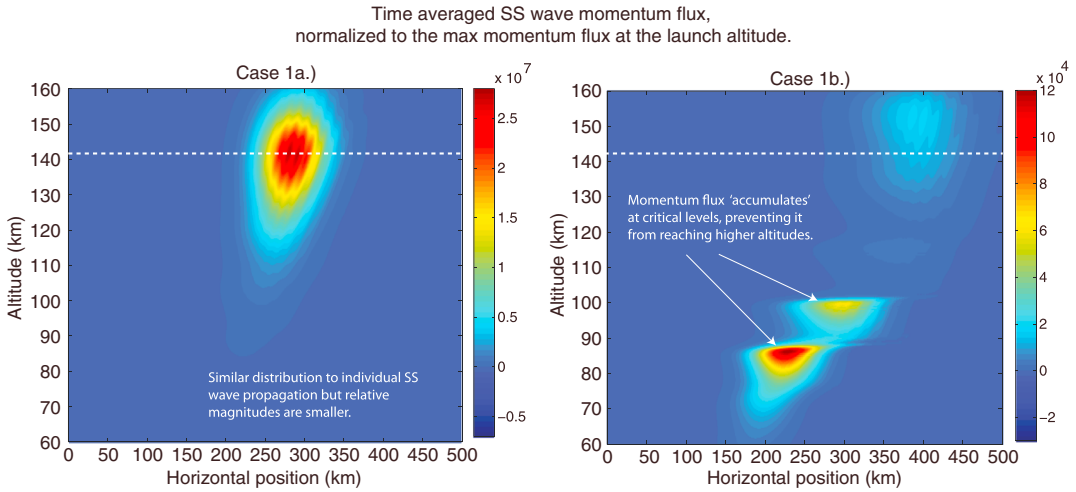

Figure 7. The time-averaged small-scale (SS) wave momentum flux, normalized to the maximum momentum flux at the launch altitude, for Cases 1a and 1b.

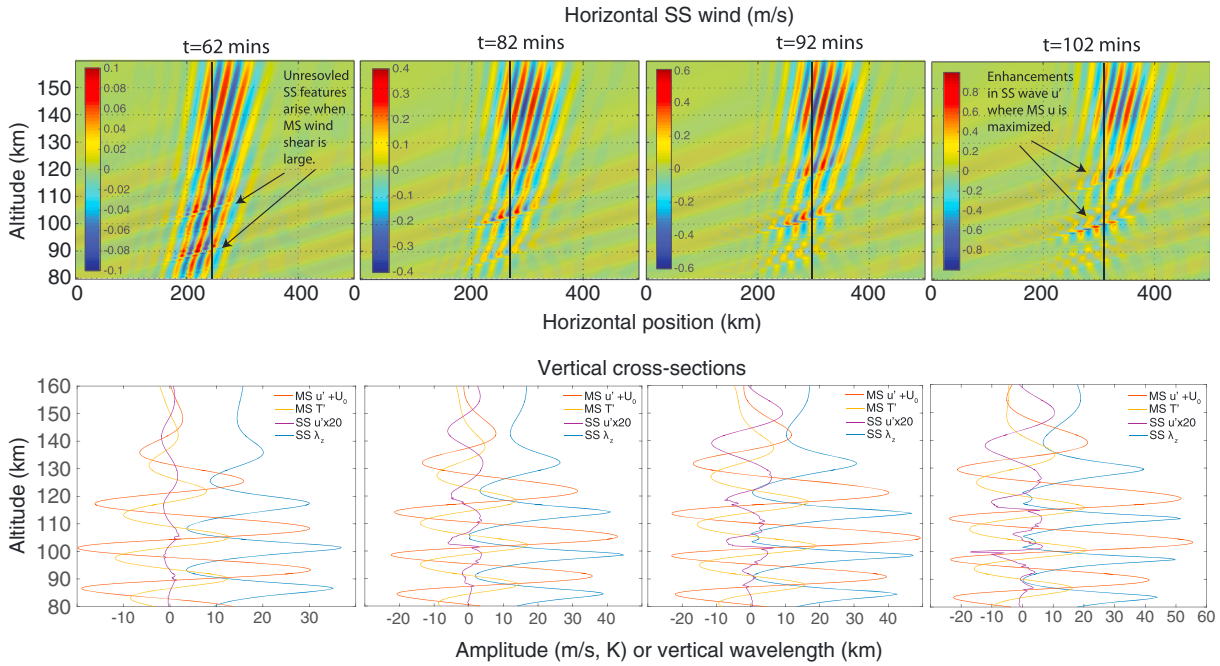

Figure 8. (top row) A time sequence of the small-scale (SS) wave horizontal wind perturbation, with the finite-amplitude medium-scale (MS) wave wind overlaid and made semitransparent for ease of comparison. (bottom row) Corresponding vertical cross sections (indicated by black line) showing the MS wind (red) and temperature (orange), the SS wave wind (multiplied by 20 for ease of comparison in purple), and the theoretical SS wave vertical wavelength (blue).

5. Case 2: Linear SS Propagation Through a Dynamic MS Wave

In this case, we excite both the SS and MS waves through the vertical body forcing described in section 2.2, rather than impose the MS wave as a static background as in Case 1. While the MS wave is of a finite amplitude, the SS wave is excited with a very small amplitude in order to limit nonlinear interactions between the waves. The MS wave is, however, able to deposit momentum into the mean flow through nonlinear interactions. This case represents an intermediate scenario between the simplified Case 1 and the fully nonlinear Case 3. The SS wavefields are extracted by subtracting the MS-only simulation, presented in section 3. We note that in reality, the SS wave is at such a small amplitude that it is effectively negligible in comparison to the effects of the MS wave; however, since most predictions are based upon linear GW theory, this is an important case to study for comparison.

Figure 8 shows the SS wave propagation at 4 times, with the MS wavefield overlaid and made semitransparent for ease of comparison. The bottom row shows corresponding vertical cross sections at the location of the vertical black line.

At t = 62 min, the SS wave initially propagates through the MS wave relatively unimpeded since the MS wave is still of relatively small amplitude compared to later times. However, enhancements in the amplitude and very small vertical scale structure are seen along the regions when the MS shear is locally maximized or minimized (corresponding to the MS wave temperature peaks and troughs). These small structures are likely MS wave instabilities, which manifest in the SS wave due to their small scales.

As time progresses, and the MS wave becomes larger in amplitude, the SS wave shows regions of amplitude enhancements around the predicted critical levels as the wave is shifted to smaller vertical scales and reductions in amplitude where the vertical wavelength is shifted to larger scales. There is also evidence of partial reflection of the SS wave, especially toward the end of the simulation. While critical levels are present from the perspective of linear theory, and the amplitude of the MS wave wind exceeds the SS wave phase speed, the model results reveal significant propagation exists at these levels, which are often considered as impenetrable boundaries for waves. This occurs for several reasons, they are as follows: (1) The SS wave is a packet with a nonmonochromatic spectrum, thus some portion of the packet can penetrate the critical levels (as they have larger phase speeds) (Heale & Snively, 2015). (2) The critical levels are transient and follow the phase progression of the MS wave; thus, the interaction time between the SS wave and the critical

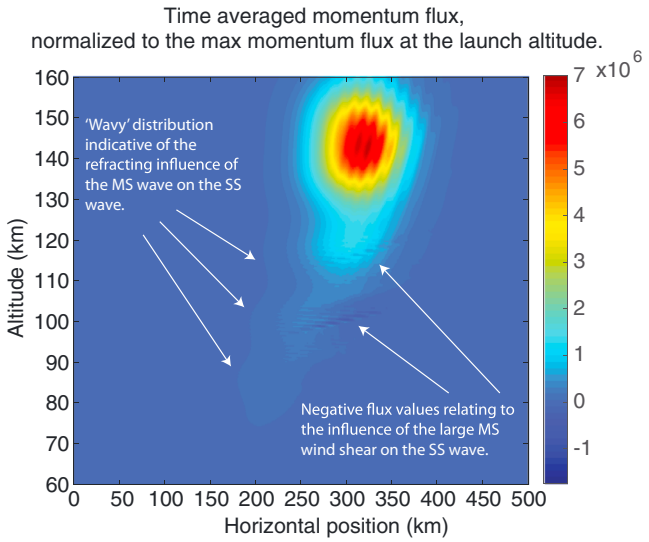

Figure 9. The time-averaged momentum flux, normalized to the peak value at the launch altitude for the small-scale (SS) wave in Case 2. MS = medium scale.

level is reduced (Eckermann, 1997; Sartelet, 2003; Senf & Achatz, 2011; Vanderhoff et al., 2008). (3) The evolution of the MS wind in time causes frequency variations in the SS wave that tend toward avoidance of filtering (Heale & Snively, 2015; Huang et al., 2013). Nevertheless, the finite-amplitude MS wave deposits its momentum into the background flow, creating a Gaussian-shaped mean flow and a permanent shear. These mean flows and shears can act to filter waves, if strong enough, as suggested in Eckermann (1997). The mean flows and shear induced by the MS wave evolve over time (as shown in Figure 3) during the SS-MS interaction; these dynamics could also affect the ground-relative frequency of the SS wave, in a method similar to that of self-acceleration. This "mutual acceleration" would depend upon the time, strength, and dynamics of the induced flow.

The timing of the wave interaction is clearly important. In this case, the higher-frequency, faster portions of the packet interact with a relatively small-amplitude MS wave early on and are able to propagate in the thermosphere. The slower packet components will be refracted and filtered to a greater extent by a larger amplitude MS wave. The enhancements in the SS wave are aligned with the tilt of the MS wave phase fronts.

Figure 9 shows the time-averaged momentum flux of the SS wave that has been normalized to the peak value at the launch altitude. The relative momentum flux has a peak value of $\sim 7 \times 10^6$ at 143 km altitude. This is 3 times less than Case 1a but around 60 times more than in Case 1b. The distribution is also different to both Cases 1a and 1b. The majority of the wave does make it up into the thermosphere, but there is a distinct MS wave modulation of the momentum flux between $z = 80$–120 km. There is also the presence of negative averaged momentum flux that occurs at the angle of the MS wave phase fronts at ~95 and 115 km. These patterns correspond to the large sheared regions of the MS wave. However, obvious critical level-induced enhancements in the momentum flux no longer occur as they did in Case 1b. Therefore, adding the full dynamics of the MS wave in this case, when compared to the static, horizontally homogeneous approximation of Case 1, noticeably affects the distribution of SS wave momentum flux.

6. Case 3: Finite-Amplitude SS Wave Propagation Through an Analytically Specified MS Wave

In this case, the SS wave is excited such that is of finite amplitude in the MLT and can evolve in a nonlinear manner. The MS wave is specified as a background wind analytically via the equation

$$U(x,z,t) = A \cdot \exp\left[-\frac{(z-(z_0+C_g(t-t_0)))^2}{2\sigma_z^2} - \frac{(x-x_0)^2}{2\sigma_x^2} + \frac{(z-z_0)}{2H}\right] \cos[k(x-x_0)+m(z-z_0)-\omega(t-t_0)] \quad (8)$$

where the parameters specified are the same as those in Table 2 with the exception of $A = 6$, $z_0 = 76$ km, $C_g = 2.7$ m/s, and $t_0 = 0$ min. The evolution of this background is shown in Figure 1a and is limited to linear propagation only, and no energy exchange occurs with the SS wave or mean flow. This is the inverse of Case 2 where the SS wave was linear and the MS wave could evolve nonlinearly. It is noted that the biggest differences between Figures 1a and 1b are that Figure 1b deposits energy into the mean flow that leads to a positive bias in the wind at late times as well as self-acceleration shifting the wave to higher frequencies above ~120 km altitude.

The evolution of the SS and MS waves for this case are presented in Figure 10. When comparing to linear Case 2, the enhancements of the SS wave amplitudes appear in similar locations aligned with the MS phase fronts; however, the SS wave now breaks where it could not in Case 2 and instead would continue to propagate upward of become partially filtered. Note that the self-acceleration effect is not captured at all in Case 2. By $t = 82$ min, instabilities begin to form near 90 and 100 km altitude, aligned with the maximum shear of the MS wave. By $t = 92$ min, the SS wave is breaking rapidly above ~120 km as a result of nonlinearity and self-acceleration. The behavior of the SS wave in this region mirrors the individual propagation of the SS wave

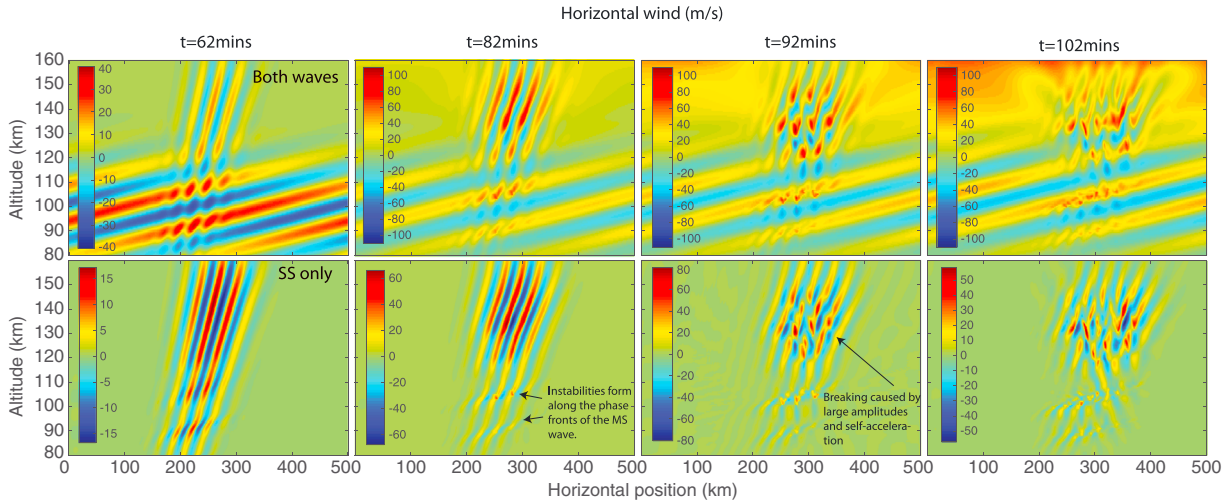

Figure 10. A time sequence (from left to right) of the horizontal winds in the case 3 simulation for (top row) both waves and (bottom row) the small-scale (SS) wave only. MS = medium scale.

presented in section 3 but is still influenced by the presence of the MS wave. The leading portion of the SS wave packet deposits momentum into the background flow that refracts the trailing edge to smaller vertical scales causing wave breaking in a region confined to the induced flow, but the SS wave packet is also refracted and influenced by the MS wave. The two regimes are clear in the panel showing just the SS wave at $t = 102$ min; below 110 km the wave breaking and deposition are influenced predominantly by the MS wave, whereas above 110 km the wave dynamics are dominated by the nonlinear deposition from the SS wave itself and resulting self-acceleration effects with a smaller influence from the MS wave.

The time-averaged, normalized momentum flux and the induced wind (mean flow) are presented in Figure 11. When comparing the normalized momentum flux to previous cases, the distribution of the momentum flux for Case 3 is a hybrid of the individual finite-amplitude propagation case in the upper half of the simulation and the linear Case 2 in the lower half. However, there are two distinct momentum flux peaks in the upper atmosphere at ~130 and 145 km altitude, whereas the individual propagation case (right-hand panel of Figure 4) showed more of a continuum; this is due to the influence of the MS wave that causes a split in the layers of momentum flux deposition. The induced wind at $t = 102$ min is also about a factor of 2 larger for Case 3 than it is for the individual propagation case, meaning that the MS wave has a significant influence in preventing the SS wave momentum and energy from reaching the upper portions of the thermosphere.

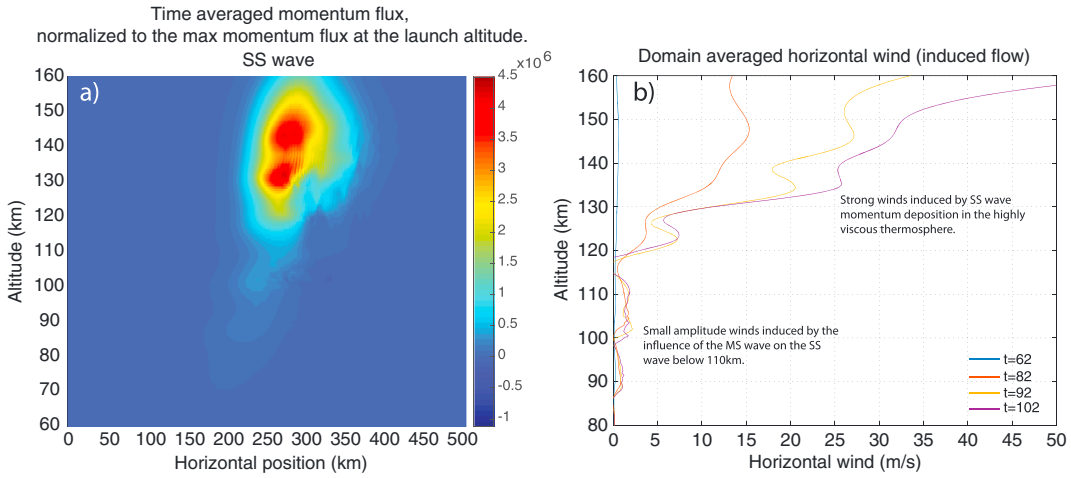

Figure 11. (a) The time-averaged momentum flux, normalized to the peak value at the launch altitude for the small-scale (SS) wave in Case 3. (b) The domain averaged horizontal wind for Case 3 at $t = 62$, 82, 92, and 102 min. MS = medium scale.

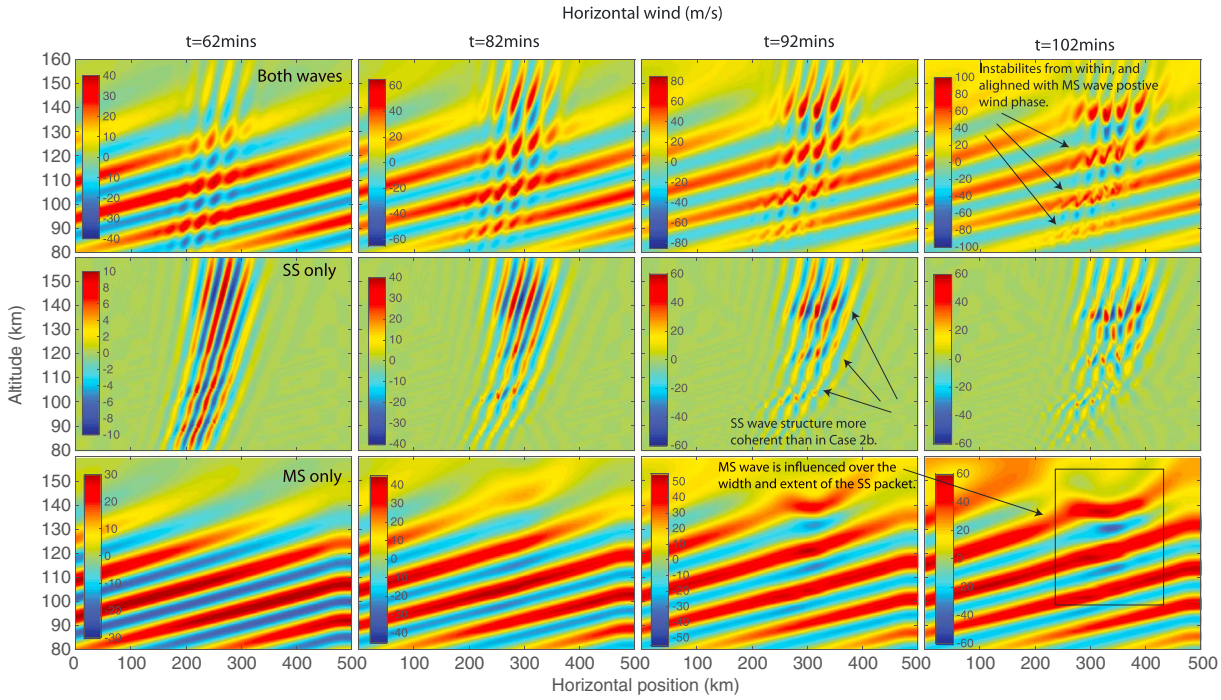

Figure 12. A time sequence (from left to right) of the horizontal winds in the finite-amplitude simulation for (top) the total wind, (middle) the SS wave only (horizontal scales less than 60 km), and (bottom) the MS wave (and anything with horizontal scales greater than 60 km).

7. Case 4: Finite-Amplitude SS and MS Wave Interactions

In the fourth and final case, the SS and MS waves are excited at finite amplitudes and can interact nonlinearly with each other and the background atmosphere. Figure 12 shows the simulation results at four different times. The waves are separated into the SS and MS components using a fourth-order Butterworth filter with a cutoff horizontal wavelength of 6 km. This cutoff was chosen by taking a Fourier transform and ensuring the split did not occur where a wave mode existed. Therefore, the SS wavefields show everything with horizontal scales less than 60 km and the MS wavefields show everything larger than 60 km. Figure 12 shows the total horizontal wind in the top row, the SS wind field in the middle row, and the MS field in the bottom row.

The early stages of the interaction show an interference pattern forming between the two waves, with enhanced and diminished SS wave amplitudes aligned with the MS phase fronts. As time progresses and the wave amplitudes get stronger, the SS wave breaks within the positive wind phases of the MS wave. Up to this point the resulting evolution is very similar between Case 3 and 4. By t = 92 min, the two simulations differ significantly above 110 km. While nonlinear effects of the MS wave were suppressed in Case 3 leading to the SS wave nonlinearity being dominant at high altitudes, the MS has a much more significant influence in Case 4. The nonlinear MS wave in Case 4 leads to a distinct vertical layering structure in the SS wavefield with enhancements at 100, 120, and 140 km altitude at t = 92 min that are far more ordered than the SS wave breaking in Case 3. In turn, the MS wavefield is distorted over the width of the SS wave packet and especially between z = 140–150 km where the SS wave is strongest and dissipation is significant. By t = 102 min, SS wave breaking can be seen within all of the positive wind phase fronts of the MS wave. Breaking at the highest altitudes (z = 135–140 km) is due to a combination of self-acceleration and the influence of the MS wave. Both the SS and MS waves have induced a mean background flow as a result of their nonlinearity (as seen by the red being stronger than the blue in Figure 12 at t = 102, top panel); this acts to refract the SS wave packet to smaller vertical scales increasing its internal shear and temperature gradients. The strong positive wind phases of the MS wave act on top of this mean flow to refract the SS wave to even smaller vertical scales causing instability to occur. The breaking of the SS wave, in turn, leads to greater energy and momentum deposition, wind shears, and induced mean flows. The MS wave is locally enhanced over the width of the SS wave, and the MS wave fronts appear almost horizontal at z = 140 km, this is likely due to secondary wave/mean flow generation caused by the dissipation and breaking of the SS wave. When comparing

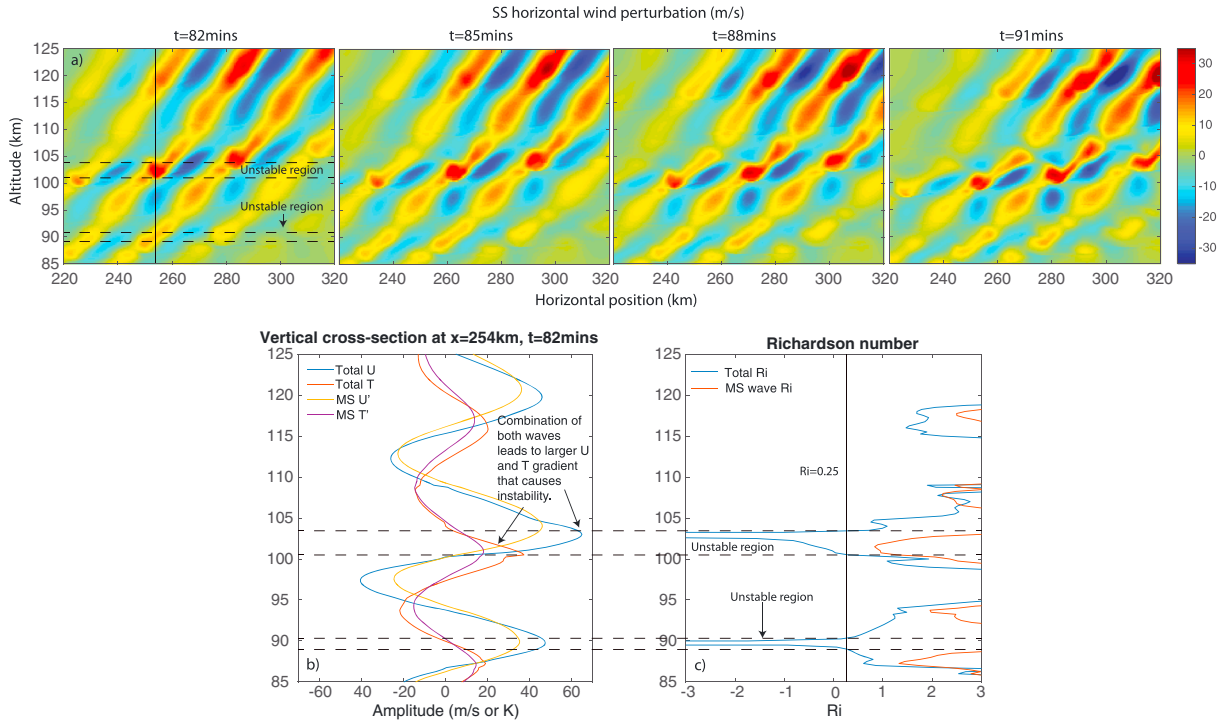

Figure 13. (a) A time sequence (from left to right) of the small-scale (SS) horizontal winds during the onset of breaking. (b) A vertical cross section of the simulation at $x = 254$ km and $t = 82$ min showing the total and medium-scale (MS) wave winds and temperatures. (c) The Richardson number plots corresponding to the profiles in Figure 13b.

to the case of the finite-amplitude SS wave propagating individually in section 2, the breaking in Case 4 occurs over a much larger altitude range, is periodic in altitude, and is aligned with the MS wave phase fronts; however, the onset of the self-acceleration induced instability occurs at roughly the same altitude.

Figure 13 provides a closer look at the onset of breaking by plotting a time sequence of the SS perturbation wind zoomed into the region of interest, along with a vertical cross section examining the wind, temperature, and Richardson numbers (Ri) at this location. The Richardson number is given by the ratio of the buoyancy frequency squared to the vertical wind shear squared $N^2/(\partial U/\partial z)^2$. Traditionally, this method is used to examine linear instability in fluids, with a negative value representing static instability (convective) and a value between 0 and 0.25 denoting shear instability (Kelvin-Helmholtz). It is noted, however, that these criteria were designed for parallel, horizontally homogeneous flow, and it is now appreciated that GW breaking can be far more complex (e.g., Achatz, 2007; Fritts et al., 2009; Sonmor & Klaassen, 1997). Nevertheless, it provides a good reference for assessing the stability of the atmosphere.

The evolution shows the SS wave having an amplitude of ~30 m/s in u' at $z = 103$ km where it is locally enhanced due to the influence of the MS wave. The wave amplitude grows slightly over the single wave period time span shown, and the phase fronts of the SS wave begin to break up. As can be seen in Figure 13b, the SS wave breaking occurs over the altitude region between where the total wind shear is maximized and the total wind itself is maximized (z ~100–104 km). This also corresponds to the region where the temperature gradient is minimized. This is similar to results seen in Heale et al. (2017). The breaking is a result of a combination of the strong MS wind refracting the SS wave to smaller scales (thus increasing the shear) and the MS wind peak corresponding with the minimum in the temperature shear, leading to a strongly reduced buoyancy frequency. It is key to note, from Figure 13c, that it is the combination of both waves that creates a classically unstable region (Richardson number <0.25); neither of the waves individually are unstable on their own. If the MS wave is considered as a background for the SS wave, the red line plot in Figure 13 shows that the minimum Richardson number is 1, whereas the combination of both waves (the blue line) is far less than zero at $z = 90$ km and between $z = 100$ and 104 km. Therefore, the interaction is crucial to the onset of breaking in this case, and the breaking occurs earlier than for the SS wave propagating individually.

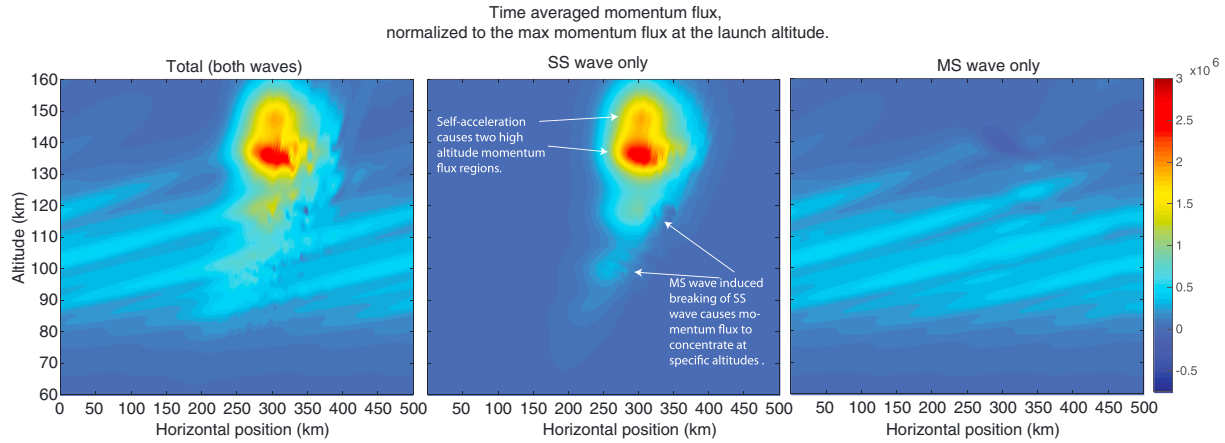

Figure 14. The time-averaged momentum flux, normalized to the peak value at the launch altitude for both waves, the small-scale (SS) wave only, and the medium-scale (MS) wave only in the finite-amplitude interaction case.

Figure 14 shows the time-averaged momentum flux normalized to the peak momentum flux at the launch altitude for the both waves, the SS wave only, and the MS wave only. The distribution is much more diffuse and less coherent than in previous cases. In particular, there are discrete regions of relatively large SS wave momentum flux centered at $z = 100$, 120, 135, and 150 km. The most interesting of which is the top two regions, which were one coherent distribution in the case of the individual SS wave propagation and split more evenly between two regions in Case 3. The splitting here is the result of the self-acceleration effect and the increasing influence of the MS wave as time progresses. The self-acceleration mechanism accelerates the leading part of the wave packet to higher altitudes as it deposits its momentum into the background flow, which in turn leads to the trailing edge of the packet being shifted to small vertical scales and breaking (e.g., due to self-acceleration instability; Fritts, Laughman, et al., 2015) that occurs at $z = 135$ km. However, in later stages, the MS wave has a large enough amplitude that it induces breaking of the SS wave at lower altitudes and thus impedes the transport of energy and momentum to the highest regions of the simulation domain. Whereas the MS wave had a small influence above 110 km in Case 3, leading to an even distribution of amplitude in the double peak structure of the momentum flux at 135 and 145 km altitude, Case 3 shows much more of the normalized momentum flux concentrated in the 135 km altitude peak.

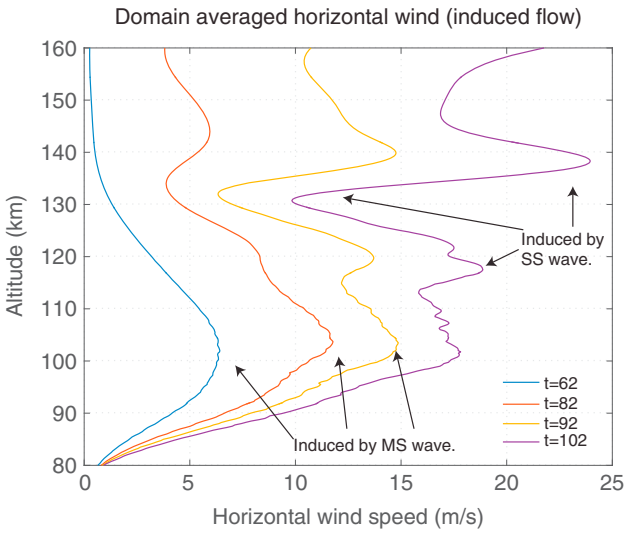

Figure 15. The horizontally domain averaged horizontal wind at four different times.

The other two local maxima in the SS wave time-averaged momentum flux occur at the altitudes where breaking forms along the MS phase fronts. The maximum value of the normalized, time-averaged momentum flux occurs lower in altitude and is one fourth of the value than in the linear case and similar in magnitude to Case 3. Comparing to the individual propagation of the finite-amplitude SS wave, the maximum value of the normalized, time-averaged momentum flux occurs at a similar height but the value is ~1000 times less. Both the individual SS wave finite-amplitude simulation and the finite-amplitude interaction show that the momentum flux distribution horizontally asymmetric, signifying that the breaking leads to significantly more complex momentum and energy distributions that are difficult to account for in GCM parameterizations. Notably, the momentum flux distribution in a real nonlinear finite-amplitude wave-wave interaction is significantly different to the static cases (Case 1) and linear case (Case 2). Also, the MS wave momentum flux is distorted by secondary wave generation and interactions with the SS wave, especially in regions where the SS wave breaks.

Finally, Figure 15 shows the horizontal domain average of the horizontal wind at 4 times shown in Figure 12. While the winds induced by the SS wave are likely to be far more localized, this method gives an indication of the induced mean flow caused by the wave-wave interaction.

At $t = 62$ min, the mean flow is dominated by the packet shape of the MS wave (as can be seen by the individual propagation of the MS wave in Figure 3). However, by 82 min, the influence of the SS wave creates a wave-like wind structure superimposed on top of the packet-shaped MS induced wind. By the end of the simulation, at $t = 102$ min, a strong shear has formed between 130 km and 140 km altitude, with the mean flow changing by 13 m/s over ~8 km. This corresponds to the altitude where the momentum flux is maximized in Figure 14 and the region where the self-acceleration instability of the SS wave occurs. There are also local peaks in the mean flow near 102 km and 118 km, with SS structure in between. Comparing the induced wind at $t = 102$ min to the individually propagating waves in Figure 3 and Case 3, the induced wind is much smaller at high altitudes in the interaction case, since the MS wave induces SS wave breaking at lower altitudes and has much more influence in impeding its progress to higher altitudes.

8. Summary and Conclusions

A 2-D nonlinear, numerical model has been used to investigate the interaction of a SS (25 km λ_x, 10 min period) and a MS wave (250 km λ_x, 90 min period) with four cases of increasing complexity. These are scales that are likely to have significant impacts on the MLT region (Fritts et al., 2014) but are not yet well resolved in typical GCM simulations (e.g., Kim et al., 2003; Liu, 2016; Liu, McInerney, Santos, et al., 2014). Those cases investigated were (1) propagation of a SS wave through static, horizontally homogeneous ambient atmospheres with an imposed MS wave feature; this case is similar to assumptions made in most GCM parameterization schemes and is especially important to understand as GCMs begin to resolve the MS wave spectrum; (2) propagation of a linear amplitude SS wave through a finite-amplitude, fully dynamic MS wave; (3) propagation of a finite-amplitude SS wave through a linear, analytically specified MS wave; and (4) the nonlinear, finite-amplitude SS and MS wave interactions, with amplitudes typical of those observed in the MLT.

When propagating individually, without the influence of the other wave, the linear amplitude SS wave is viscously dissipated in the thermosphere. By comparison, the finite-amplitude SS wave undergoes self-acceleration and associated wave breaking, inducing mean flows of up to 50 m/s at $z = 150$ km. The MS wave also, when alone, induces a packet-shaped mean flow with peak amplitudes of up to 15 m/s over the time scales simulated.

For Case 1, two background atmospheric states were chosen to represent the MS at different fixed times in its propagation. The first represents the state of the MS wave at the launch time of the SS wave. In this case, the MS wave had relatively small peak amplitudes of 10 m/s and 5 K and the SS wave propagated through the MS wave with little refraction or filtering and dissipated in the thermosphere. The second state was after the MS wave had propagated to higher altitudes and grown in amplitude. In this case the SS wave was strongly critical level filtered by the strong winds associated with the MS wave, and very little of the wave energy and momentum could reach the altitudes where it is strongly dissipated by molecular viscosity. The two static representations of the MS wave at two different times produced vastly different SS wave propagation and momentum flux distributions, indicating that reducing a dynamic wave interaction to a static representation can produce very variable results depending upon the state of the larger-scale wave at the time the background is frozen and greatly simplifies the physics.

In Case 2, the full MS wave dynamics were included, leading to refraction, reflection, and filtering of the SS wave, which became more prominent over time as the MS wave grew stronger in amplitude. In particular, the SS wave is refracted to smaller vertical scales in the positive wind phases of the MS wave and refracted to larger scales in the negative wind phase of the MS wave. The inclusion of the time dependence of the MS wave leads to reduced critical level filtering in comparison to a static representation of the MS wave at the same amplitude. This effect is due to transience of the critical level and an induced shift in the SS wave's ground-relative frequency by the time-dependent MS wave and has been demonstrated in previous studies (e.g., Eckermann, 1997; Heale & Snively, 2015; Huang et al., 2013; Sartelet, 2003; Vanderhoff et al., 2008). However, while transience leads to reduced critical level filtering, the finite-amplitude MS wave is continuously depositing part of its momentum and energy into a permanent mean flow and shear, which, if large enough, can cause more permanent critical levels.

In Case 3, the SS wave is excited such that is reaches finite amplitudes in the MLT and can evolve nonlinearly; however, the MS wave is specified analytically so that it does not exhibit nonlinearity or energy exchange between it and the SS wave or the mean flow. Below 110 km, the MS wave heavily influences the momentum flux deposition of the SS wave by causing the MS wave to break along the phase fronts of the MS wave

where the shear is maximum. Above 110 km, the influence of the MS wave on the SS wave is relatively weak (compared to Case 4) and breaking and momentum deposition is dominated by self-acceleration effects and dissipation due to molecular viscosity and thermal conductivity. While this case is far from perfect, it provides the best representation of the fully nonlinear, time-dependent interaction presented in Case 4.

In Case 4, both waves are of finite amplitude leading to nonlinear interactions and breaking of the SS wave. The SS wave breaks predominately within the positive wind phases of the MS wave between where the wind shear is maximized and the temperature gradient is minimized, this is also where the SS wave is refracted to small vertical scales. This leads to an induced mean flow that is wave-like in altitude. It is also noted that both waves individually are classical stable when assessing their Richardson numbers, but it is the total of both waves interacting that leads to instability. Due to the SS wave breaking, far less of the SS wave energy and momentum is able to propagate as high as it can in the linear case or if it propagates individually. The time-averaged, normalized momentum flux distribution has a number of distinct peaks but is generally far more diffuse, complex, and asymmetric than the previous cases. Self-acceleration induced breaking is also present in Case 4, which is not captured in the linear scenario and, in conjunction with MS wave influences, leads to a large permanent shear in the mean flow between 130 and 140 km altitude. However, the induced winds are far smaller than for the finite-amplitude SS wave propagating individually or for Case 2.

The finite-amplitude simulation leads to feedback between waves, secondary wave generation, breaking and turbulence that occurs preferentially within regions of the atmosphere, in addition to significant permanent mean flows and shears, and a more complex momentum flux distribution than when considering linear propagation alone. While this paper only demonstrates nonlinear wave interactions under very specific cases, it is clear that there are important mechanisms that static and linear assumptions are unable to reproduce and that are unlikely to be well represented in parameterization schemes that do not include transience, horizontal inhomogeneity, and nonlinear feedback mechanisms between waves and the mean flow. Primary conclusions are the following.

1. The MS wave can evolve significantly over the time it takes a SS wave to propagate into the thermosphere. Therefore, considering a MS wave as stationary, relative to the SS waves, and assuming instant propagation of the SS wave from the source to thermosphere significantly simplifies the physics. This shows the importance of including transience for accurately capturing interactions.
2. Linear assumptions and lack of transience neglect crucial self-acceleration, mutual acceleration, and breaking/wave feedback effects. As a result, they do not adequately capture the momentum flux distribution resulting from SS and MS wave interactions. Even for waves with modest amplitudes in the mesopause region (a few K), amplitudes can be large in the lower thermosphere, leading to significant nonlinearity.
3. Fully nonlinear interactions lead to breaking and momentum deposition angled along the phase fronts of the MS wave, preferentially occurring where the wave temperature gradient is minimized and the velocity is maximized. The MS wave is also significantly modulated over the region of the SS wave packet, and significant background flows and shears are produced as a result of the interaction.

Results strongly suggest a need to capture time-dependent MS effects on SS waves, and vice-versa in future partially resolved GCM parameterizations. The need for transience and a move away from the single column approach are crucial for improving these schemes. The results in this paper support the conclusions of Senf and Achatz (2011), Ribstein et al. (2015), and Bölöni et al. (2016) who found that using ray tracing techniques with WKB theory to include time dependence and horizontal propagation led to much better agreement with large eddy simulations models on wave-mean flow interactions. It is noted that typical operational parameterizations work statistically and consider a broad spectrum of waves. In contrast, this study looks at simplified quasi-monochromatic interactions. In order to gain some understanding of the fundamental physical processes behind these types of interactions, under different limits, we have deliberately kept the case studies simple. As the next generation of GCMs partially resolve and partially parameterize the GW spectrum, studying the physics needed to represent interactions between the small scales (which will remain parameterized) and the medium scales (which will become resolved) will become important.

Acknowledgments
Research by C. J. Heale and J. B. Snively was supported under NSF grants AGS-1344356 and AGS-1151746. The authors thank three anonymous reviewers and the Editor for reviewing and suggesting improvements to this publication. Simulation data needed to reproduce the figures will be archived at ERAU for 5 years and are available on request to the authors at healec@erau.edu.

References

Achatz, U. (2007). Gravity-wave breaking: Linear and primary nonlinear dynamics. *Advances in Space Research*, *40*, 719–733.

Akmaev, R. A. (2001). Simulation of large-scale dynamics in the mesosphere and lower thermosphere with the Doppler-spread parameterization of gravity waves: 1. Implementation and zonal mean climatologies. *Journal of Geophysical Research*, *106*(D1), 1193–1204. https://doi.org/10.1029/2000JD900520

Alexander, M. J., & Dunkerton, T. J. (1999). A spectral parameterization of mean-flow forcing due to breaking gravity waves. *Journal of the Atmospheric Sciences*, *56*, 4167–4182.

Alexander, M. J., Geller, M., McLandress, C., Polavarapu, S., Preusse, P., Sassi, F., … Watanabe, S. (2010). Recent developments in gravity-wave effects in climate models and the global distribution of gravity-wave momentum flux from observations and models. *Quarterly Journal of the Royal Meteorological Society*, *136*(650), 1103–1124. https://doi.org/10.1002/qj.637

Amemiya, A., & Sato, K. (2016). A new gravity wave parameterization including three-dimensional propagation. *Journal of the Meteorological Society of Japan*, *94*(3), 237–256.

Bale, D. S., LeVeque, R. J., Mitran, S., & Rossmanith, J. A. (2002). A wave propagation method for conservation laws and balance laws with spatially varying flux functions. *Journal on Scientific Computing*, *24*(3), 955–978.

Becker, E. (2009). Sensitivity of the upper mesosphere to the Lorenz energy cycle of the troposphere. *Journal of the Atmospheric Sciences*, *66*(3), 647–666. https://doi.org/10.1175/2008JAS2735.1

Bölöni, G., Ribstein, B., Muraschko, J., Sgoff, C., Wei, J., & Achatz, U. (2016). The interaction between atmospheric gravity waves and large-scale flows: An efficient description beyond the nonacceleration paradigm. *Journal of the Atmospheric Sciences*, *73*(12), 4833–4852. https://doi.org/10.1175/JAS-D-16-0069.1

Booker, J. R., & Bretherton, F. P. (1967). The critical layer for internal gravity waves in a shear flow. *Journal of Fluid Mechanics*, *27*, 513–539.

Bossert, K., Fritts, D. C., Pautet, P.-D., Williams, B. P., Taylor, M. J., Kaifler, B., … MacKinnon, A. D. (2015). Momentum flux estimates accompanying multiscale gravity waves over Mount Cook, New Zealand, on 13 July 2014 during the DEEPWAVE campaign. *Journal of Geophysical Research: Atmospheres*, *120*, 9323–9337. https://doi.org/10.1002/2015JD023197

Broutman, D., & Young, W. (1986). On the interaction of small-scale oceanic internal waves with near-inertial waves. *Journal of Fluid Mechanics*, *166*, 341–358.

Chen, C.-C., Durran, D. R., & Hakim, G. J. (2005). Mountain-wave momentum flux in an evolving synoptic-scale flow. *Journal of the Atmospheric Sciences*, *62*, 3213–3231. https://doi.org/10.1175/JAS3543.1

de la Cámara, A., Lott, F., & Hertzog, A. (2014). Intermittency in a stochastic parameterization of nonorographic gravity waves. *Journal of Geophysical Research: Atmospheres*, *119*, 11,905–11,919. https://doi.org/10.1002/2014JD022002

Dosser, H. V., & Sutherland, B. R. (2011). Weakly nonlinear non-Boussinesq internal gravity wavepackets. *Journal of Physics D*, *240*, 346–356.

Dunkerton, T. J., & Fritts, D. C. (1984). Transient gravity-wave critical layer interaction Part I: Convective adjustment and the mean zonal acceleration. *Journal of the Atmospheric Sciences*, *41*, 992–1007.

Eckermann, S. D. (1997). Influence of wave propagation on the Doppler spreading of atmospheric gravity waves. *Journal of the Atmospheric Sciences*, *54*, 2554–2573.

Fomichev, V. I., Ward, W. E., Beagley, S. R., McLandress, C., McConnell, J. C., McFarlane, N. A., & Shepherd, T. G. (2002). Extended Canadian middle atmosphere model: Zonal-mean climatology and physical parameterizations. *Journal of Geophysical Research*, *107*(D10), 4087. https://doi.org/10.1029/2001JD000479

Fritts, D., & Alexander, M. J. (2003). Gravity wave dynamics and effects in the middle atmosphere. *Reviews of Geophysics*, *41*(1), 1003. https://doi.org/10.1029/2001RG000106

Fritts, D. C. (1984). Gravity wave saturation in the middle atmosphere: A review of theory and observations. *Reviews of Geophysics*, *22*, 275–308.

Fritts, D. C., & Dunkerton, T. J. (1985). Fluxes of heat and constituents due to convectively unstable gravity waves. *Annales Geophysicae*, *68*, 247–265.

Fritts, D. C., & Lund, T. S. (2011). Gravity wave influences in the thermosphere and ionosphere: Observations and recent modeling. In *Aeronomy of the Earth's Atmosphere and Ionosphere* (pp. 109–130). Netherlands: Springer.

Fritts, D. C., Garten, J. F., & Andreasson, O. (1996). Wave breaking and transition to turbulence in stratified shear flows. *Journal of the Atmospheric Sciences*, *53*, 1057–1085.

Fritts, D. C., Laughman, B., Lund, T. S., & Snively, J. B. (2015). Self-acceleration and instability of gravity wave packets: 1. Effects of temporal localization. *Journal of Geophysical Research: Atmospheres*, *120*, 8783–8803. https://doi.org/10.1002/2015JD023363

Fritts, D. C., Pautet, P.-D., Bossert, K., Taylor, M. J., Williams, B. P., Limura, H., … Stober, G. (2014). Quantifying gravity wave momentum fluxes with mesosphere temperature mappers and correlative instrumentation. *Journal of Geophysical Research: Atmospheres*, *119*, 13,583–13,603. https://doi.org/10.1002/2014JD022150

Fritts, D. C., Smith, R. B., Taylor, M. J., Doyle, J. D., Eckermann, S. D., Dörnbrack, A., … Ma, J. (2015). The deep propagating gravity wave experiment (DEEPWAVE): An airborne and ground-based exploration of gravity wave propagation and effects from their sources throughout the lower and middle atmosphere. *American Meteorological Society*, *97*, 425–453. https://doi.org/10.1175/BAMS-D-14-00269.1

Fritts, D. C., Vadas, S. L., Wan, K., & Werne, J. A. (2006). Mean and variable forcing of the middle atmosphere by gravity waves. *Journal of Atmospheric and Solar-Terrestrial Physics*, *68*, 247–265.

Fritts, D. C., Wang, L., Werne, J., Lund, T., & Wan, K. (2009). Gravity wave instability and dynamics at high Reynolds numbers. Part I: Wave field evolution at large amplitudes and high frequencies. *Journal of the Atmospheric Sciences*, *66*, 1126–1147.

Garcia, R. R., & Boville, B. A. (1994). Downward control of the mean meridional circulation and temperature distribution of the polar winter stratosphere. *Journal of the Atmospheric Sciences*, *51*, 2238–2245. https://doi.org/10. 1175/1520-0469(1994)051

Garcia, R. R., Marsh, D. R., Kinnison, D. E., Boville, B. A., & Sassi, F. (2007). Simulations of secular trends in the middle atmosphere. *Journal of Geophysical Research*, *112*, D09301. https://doi.org/10.1029/2006JD007485

Hasha, A., Bühler, O., & Scinocca, J. (2008). Gravity wave refraction by three-dimensionally varying winds and the global transport of angular momentum. *Journal of the Atmospheric Sciences*, *65*, 2892–2906. https://doi.org/10.1175/2007JAS2561.1

Heale, C. J., Bossert, K., Snively, J. B., Fritts, D. C., Pautet, P.-D., & Taylor, M. J. (2017). Numerical modeling of a multiscale gravity wave event and its airglow signatures over Mount Cook, New Zealand, during the DEEPWAVE campaign. *Journal of Geophysical Research: Atmospheres*, *122*, 846–860. https://doi.org/10.1002/2016JD025700

Heale, C. J., & Snively, J. B. (2015). Gravity wave propagation through a vertically and horizontally inhomogeneous background wind. *Journal of Geophysical Research: Atmospheres*, *120*, 5931–5950. https://doi.org/10. 1002/2015JD023505

Heale, C. J., Snively, J. B., & Hickey, M. P. (2014). Numerical simulation of the long range propagation of gravity wave packets at high latitudes. *Journal of Geophysical Research: Atmospheres*, *119*, 11,116–11,134. https://doi.org/10.1002/2014JD022099

Heale, C. J., Snively, J. B., Hickey, M. P., & Ali, C. J. (2014). Thermospheric dissipation of upward propagating gravity wave packets. *Journal of Geophysical Research: Space Physics*, *119*, 3857–3872. https://doi.org/10.1002/2013JA019387

Hickey, M., & Cole, K. (1988). A numerical model for gravity wave dissipation in the thermosphere. *Journal of Atmospheric and Terrestrial Physics*, *50*(8), 689–697. https://doi.org/10.1016/0021-9169(88) 90032-3

Hines, C. O. (1997). Doppler-spread parameterization of gravity-wave momentum deposition in the middle atmosphere. 1. Basic formulation. *Journal of Atmospheric and Solar-Terrestrial Physics*, *59*, 371–386.
Hocke, K., & Tsuda, T. (2001). Gravity waves and ionospheric irregularities over tropical convection zones observed by GPS/MET radio occultation. *Geophysical Research Letters*, *28*, 2815–2818.
Holton, J. R. (1982). The role of gravity wave induced drag and diffusion in the momentum budget of the mesosphere. *Journal of the Atmospheric Sciences*, *39*, 791–799.
Holton, J. R. (1983). The influence of gravity wave breaking on the general circulation of the middle atmosphere. *Journal of the Atmospheric Sciences*, *40*, 2497–2507.
Huang, C. M., Zhang, S. D., Yi, F., Huang, K. M., Zhang, Y. H., Gan, Q., & Gong, Y. (2013). Frequency variations of gravity waves interacting with a time-varying tide. *Annales Geophysicae*, *31*, 1731–1743. https://doi.org/10.5194/angeo-31-1731-2013
Huang, K. M., Zhang, S. D., Yi, F., Huang, C. M., Gan, Q., Gong, Y., & Zhang, Y. H. (2014). Nonlinear interaction of gravity waves in a nonisothermal and dissipative atmosphere. *Annales Geophysicae*, *32*, 263–275. https://doi.org/10.1002/2015JA021349
Hung, R. J., & Kuo, J. P. (1978). Ionospheric observations of gravity-waves associated with hurricane Eloise. *Journal of Geophysical Research*, *45*, 67–80.
Kelley, M. C. (1997). situ ionospheric observations of severe weather-related gravity waves and associated small-scale plasma structure. *Journal of Geophysical Research*, *102*, 329–336.
Kim, Y. J., Eckermann, S. D., & Chun, H. Y. (2003). A overview of the past, present, and future of gravity wave drag parameterization for numerical climate and weather prediction models. *Atmosphere-Ocean*, *41*, 65–98.
LeVeque, R. J., & Berger, M. J. (2004). Clawpack software version 4.2. Retrieved from https://www.clawpack.org
Li, T., She, C. Y., Liu, H. L., & Montgomery, M. T. (2007). Evidence of a gravity wave breaking event and the estimation of the wave characteristics from sodium lidar observation over Fort Collins, CO (41°N, 105°W). *Geophysical Research Letters*, *34*, L05815. https://doi.org/10.1029/2006GL028,988
Lighthill, J. (1978). *Waves in fluids*. Cambridge, UK: Cambridge University Press.
Lindzen, R. S. (1973). Wave-mean flow interactions in the upper mesosphere. *Boundary-Layer Meteorology*, *4*, 327–343.
Lindzen, R. S. (1981). Turbulence and stress owing gravity wave and tidal breakdown. *Journal of Geophysical Research*, *86*(C10), 9707–9714.
Liu, A. Z., Lu, X., & Franke, S. J. (2013). Diurnal variation of gravity wave momentum flux and its forcing on the diurnal tide. *Journal of Geophysical Research: Atmospheres*, *118*, 1668–1678. https://doi.org/10.1029/2012JD018653
Liu, H.-L. (2016). Variability and predictability of the space environment as related to lower atmosphere forcing. *Space Weather*, *14*, 634–658. https://doi.org/10.1002/2016SW001450
Liu, H.-L., McInerney, J. M., Santos, S., Lauritzen, P. H., Taylor, M. A., & Pedatella, N. M. (2014). Gravity waves simulated by high-resolution Whole Atmosphere Community Climate Model. *Geophysical Research Letters*, *41*, 9106–9112. https://doi.org/10.1002/2014GL062468
Liu, X., Xu. J., & Liu, H. L. (2008). Nonlinear interactions between gravity waves with different wavelengths and diurnal tide. *Journal of Geophysical Research*, *113*, D08112. https://doi.org/10.1029/2007JD009136
Liu, X., Xu, J., Liu, H. L., Yue, J., & Yuan, W. (2014). Simulations of large winds and wind shears induced by gravity wave breaking in the mesosphere and lower thermosphere (MLT) region. *Annales Geophysicae*, *32*, 543–552. https://doi.org/10.5194/angeo-32-543-2014
Liu, X., Xu, J., Yue, J., Liu, H. L., & Yuan, W. (2014). Large winds and wind shears caused by the nonlinear interactions between gravity waves and tidal backgrounds in the mesosphere and lower thermosphere. *Journal of Geophysical Research: Space Physics*, *119*, 7698–7708. https://doi.org/10.1002/2014JA020221
Liu, X., Xu, J., Yue, J., & Vadas, S. L. (2013). Numerical modeling study of the momentum deposition of small amplitude gravity waves in the thermosphere. *Annales Geophysicae*, *31*, 1–14.
Lu, X., Chen, C., Huang, W., Smith, J. A., Chu, X., Yuan, T., … Chihoko Y. (2015). A coordinated study of 1?h mesoscale gravity waves propagating from Logan to Boulder with CRRL Na Doppler lidars and temperature mapper. *Journal of Geophysical Research: Atmospheres*, *120*, 10,006–10,021. https://doi.org/10.1002/2015JD023604
Lu, X., Chu, X., Li, H., Chen, C., Smith, J. A., & Vadas, S. L. (2017). Statistical characterization of high-to-medium frequency mesoscale gravity waves by lidar-measured vertical winds and temperatures in the MLT. *Journal of Atmospheric and Solar-Terrestrial Physics*, *162*(Supplement C), 3–15. https://doi.org/10.1016/j.jastp.2016.10.009
Lu, X., Liu, H.-L., Liu, A. Z., Yue, J., McInerney, J. M., & Li, Z. (2012). Momentum budget of the migrating diurnal tide in the Whole Atmosphere Community Climate Model at vernal equinox. *Journal of Geophysical Research*, *117*, D07112. https://doi.org/10.1029/2011JD017,089
Lund, T. S., & Fritts, D. C. (2012). Numerical simulation of gravity wave breaking in the lower thermosphere. *Journal of Geophysical Research*, *117*, D21105. https://doi.org/10.1029/2012JD017536
Matsuno, T. (1982). A quasi one-dimensional model of the middle atmosphere circulation interacting with internal gravity waves. *Journal of the Meteorological Society of Japan*, *60*, 215–226.
Meyer, C. K. (1999). Gravity wave interactions with the diurnal propagating tide. *Journal of Geophysical Research*, *104*, 4223–4239.
Moffat-Griffin, T., Taylor, M. J., Nakamura, T., Kavanagh, A. J., Hosking, J. S., & Orr, A. (2017). 3rd ANtarctic Gravity Wave Instrument Network (ANGWIN) science workshop. *Advances in Atmospheric Sciences*, *34*(1), 1–3. https://doi.org/10.1007/s00376-016-6197-5
Nastrom, G. D., & Fritts, D. (1992). Sources of mesoscale variability of gravity waves. Part I. Topographic excitation. *Journal of the Atmospheric Sciences*, *49*, 101–110.
Nielsen, K., Talor, M., Hibbins, R., & Jarvis, M. (2009). Climatology of short-period mesospheric gravity waves over Halley, Antarctica (76S, 27W). *Journal of Atmospheric and Solar-Terrestrial Physics*, *71*, 991–1000.
Nielsen, K., Taylor, M., Hibbins, R., Jarvis, M., & Russel III, J. M. (2012). On the nature of short-period mesospheric gravity wave propagation over Halley, Antarctica. *Journal of Geophysical Research*, *117*, D05124. https://doi.org/10.1029/2011JD016261
Pautet, P., Talyor, M., Liu, A., & Swenson, G. (2005). Climatology of short-period gravity waves observed over northern Australia during the Darwin Area Wave Experiment (DAWEX) and their dominant source regions. *Journal of Geophysical Research*, *110*, D03S90. https://doi.org/10.1029/2004JD004954
Pitteway, M. L. V., & Hines, C. O. (1963). The viscous damping of atmospheric gravity waves. *Canadian Journal of Physics*, *41*, 1935–1948.
Ribstein, B., Achatz, U., & Senf, F. (2015). The interaction between gravity waves and solar tides: Results from 4-D ray tracing coupled to a linear tidal model. *Journal of Geophysical Research: Space Physics*, *120*, 6795–6817. https://doi.org/10.1002/2015JA021349
Sartelet, K. N. (2003). Wave propagation inside an inertial wave. Part I: Role of time dependence and scale separation. *Journal of the Atmospheric Sciences*, *60*(12), 1433–1447.
Sato, K., Tateno, S., Watanabe, S., & Kawatani, Y. (2012). Gravity wave characteristics in the Southern Hemisphere revealed by a high-resolution middle-atmosphere general circulation model. *Journal of the Atmospheric Sciences*, *69*(4), 1378–1396. https://doi.org/10.1175/JAS-D-11-0101.1

Schmidt, H., Brasseur, G. P., Charron, M., Manzini, E., Giorgetta, M. A., Diehl, T., … Walters, S. (2006). The HAMMONIA chemistry climate model: Sensitivity of the mesopause region to the 11-year solar cycle and CO_2 doubling. *Journal of Climate*, *19*(16), 3903–3931. https://doi.org/10.1175/JCLI3829.1

Scinocca, J. F., & Sutherland, B. R. (2010). Self-acceleration in the parameterization of orographic gravity wave drag. *Journal of the Atmospheric Sciences*, *67*, 2537–2546. https://doi.org/10.1175/2010JAS3358.1

Senf, F., & Achatz, U. (2011). On the impact of middle-atmosphere thermal tides on the propagation and dissipation of gravity waves. *Journal of Geophysical Research*, *116*, D24110. https://doi.org/10.1029/2011JD015794

Snively, J. B. (2013). Mesospheric hydroxyl airglow signatures of acoustic and gravity waves generated by transient tropospheric forcing. *Geophysical Research Letters*, *40*, 1–5. https://doi.org/10.1002/grl.50886

Snively, J. B., & Pasko, V. P. (2008). Excitation of ducted gravity waves in the lower thermosphere by tropospheric sources. *Journal of Geophysical Research*, *113*, A06303. https://doi.org/10.1029/2007JA012693

Song, I.-S., & Chun, H.-Y. (2008). A Lagrangian spectral parameterization of gravity wave drag induced by cumulus convection. *Journal of the Atmospheric Sciences*, *65*(4), 1204–1224. https://doi.org/10.1175/2007JAS2369.1

Sonmor, L. J., & Klaassen, G. P. (1997). Toward a unified theory of gravity wave stability. *Journal of the Atmospheric Sciences*, *54*, 2655–2680.

Sutherland, B. R. (2001). Finite-amplitude internal wavepacket dispersion and breaking. *Journal of Fluid Mechanics*, *429*, 343–380.

Sutherland, B. R. (2006). Weakly nonlinear internal gravity wavepackets. *Journal of Fluid Mechanics*, *569*, 249–258.

Suzuki, S., Nakamura, T., Ejiri, M. K., Tsutsumi, M., Shiokawa, K., & Kawahara, T. D. (2010). Simultaneous airglow, lidar, and radar measurements of mesospheric gravity waves over Japan. *Journal of Geophysical Research*, *115*, D24113. https://doi.org/10.1029/2010JD014674

Suzuki, S., Shiokawa, K., Otsuka, Y., Ogawa, T., & Wilkinson, P. (2004). Statistical characteristics of gravity waves observed by an all-sky imager at Darwin, Australia. *Journal of Geophysical Research*, *109*, D20S07. https://doi.org/10.1029/2003JD004336

Taylor, M. J., Pautet, P. D., Medeiros, A. F., Buriti, R., Fechine, J., Fritts, D. C., … Sao Sabbas, F. T. (2009). Characteristics of mesospheric gravity waves near the magnetic equator, Brazil, during the SpreadFEx campaign. *Annales Geophysicae*, *27*, 461–472. https://doi.org/10.5194/angeo-27-461-2009

Vadas, S. L. (2007). Horizontal and vertical propagation and dissipation of gravity waves in the thermosphere from lower atmospheric and thermospheric sources. *Journal of Geophysical Research*, *112*, A06305. https://doi.org/10.1029/2006JA011845

Vadas, S. L., & Fritts, D. C. (2005). Thermospheric responses to gravity waves: Influences of increasing viscosity and thermal diffusivity. *Journal of Geophysical Research*, *110*, D15103. https://doi.org/10.1029/2004JD005574

Vadas, S. L., & Fritts, D. C. (2006). Influence of solar variability on gravity wave structure and dissipation in the thermosphere from tropospheric convection. *Journal of Geophysical Research*, *111*, A10S12. https://doi.org/10.1029/2005JA011510

Vadas, S. L., & Liu, H. L. (2009). Generation of large scale gravity waves and neutral winds in the thermosphere from the dissipation of convectively generated gravity waves. *Journal of Geophysical Research*, *114*, A10310. https://doi.org/10.1029/2009JA014108

Vanderhoff, J. C., Nomura, K. K., Rottman, J. W., & Macaskill, C. (2008). Doppler spreading of internal gravity waves by an inertia-wave packet. *Journal of Geophysical Research*, *113*, C05018. https://doi.org/10.1029/2007JC004390

Vincent, R. A., & Reid, I. M. (1983). HF Doppler measurements of mesospheric momentum fluxes. *Journal of the Atmospheric Sciences*, *40*, 1321–1333.

Warner, C. D., & McIntyre, M. E. (2001). An ultra simple spectral parameterization for non-orographic gravity waves. *Journal of the Atmospheric Sciences*, *58*, 1837–1857.

Watanabe, S., & Miyahara, S. (2009). Quantification of the gravity wave forcing of the migrating diurnal tide in a gravity wave–resolving general circulation model. *Journal of Geophysical Research*, *114*, D07110. https://doi.org/10.1029/2008JD011218

Waterscheid, R. L., & Hickey, M. P. (2011). Group velocity and energy flux in the thermosphere: Limits on the validity of group velocity in a viscous atmosphere. *Journal of Geophysical Research*, *116*, D12101. https://doi.org/10.1029/2010JD014987

Yamada, Y., Fukunishi, H., Nakamura, T., & Tsuda, T. (2001). Breaking of small-scale gravity wave and transition to turbulence observed in OH airglow. *Journal of Geophysical Research*, *28*(11), 2153–2156.

Yiğit, E., Aylward, A. D., & Medvedev, A. S. (2008). Parameterization of the effects of vertically propagating gravity waves for thermosphere general circulation models: Sensitivity study. *Journal of Geophysical Research*, *113*, D19106. https://doi.org/10.1029/2008JD010135

Yiğit, E., & Medvedev, A. S. (2009). Heating and cooling of the thermosphere by internal gravity waves. *Geophysical Research Letters*, *36*, L14807. https://doi.org/10.1029/2009GL038507

Yigit, E., & Medvedev, A. S. (2010). Internal gravity waves in the thermosphere during low and high solar activity: Simulation study. *Journal of Geophysical Research*, *115*, A00G02. https://doi.org/10.1029/2009JA015106

Yiğit, E., & Medvedev, A. S. (2015). Internal wave coupling processes in Earth's atmosphere. *Advances in Space Research*, *55*, 983–1003. https://doi.org/10.1016/j.asr.2014.11.020

Yiğit, E., & Medvedev, A. S. (2016). Role of gravity waves in vertical coupling during sudden stratospheric warmings. *Geoscience Letters*, *3*(1), 27.

Yiğit, E., & Medvedev, A. S. (2017). Influence of parameterized small-scale gravity waves on the migrating diurnal tide in Earth's thermosphere. *Journal of Geophysical Research: Space Physics*, *122*, 4846–4864. https://doi.org/10.1002/2017JA024089

Yiğit, E., Medvedev, A. S., Aylward, A. D., Hartogh, P., & Harris, M. J. (2009). Modeling the effects of gravity wave momentum deposition on the general circulation above the turbopause. *Journal of Geophysical Research*, *114*, D07101. https://doi.org/10.1029/2008JD011132

Yiğit, E., Medvedev, A. S., Aylward, A. D., Ridley, A. J., Harris, M. J., Moldwin, M. B., & Hartogh, P. (2012). Dynamical effects of internal gravity waves in the equinoctial thermosphere. *Journal of Atmospheric and Solar-Terrestrial Physics*, *90-91*(Supplement C), 104–116. https://doi.org/10.1016/j.jastp.2011.11.014

Yuan, T., Heale, C. J., & Snively, J. B. (2016). Evidence of spectrally broad gravity wave packet propagation and dispersion in the mesopause region observed by the Na lidar and Mesospheric Temperature Mapper above Logan, Utah. *Journal of Geophysical Research*, *121*, 579–594. https://doi.org/10.1002/2015JD023685

Zettergren, M. D., & Snively, J. B. (2015). Ionospheric response to infrasonic-acoustic waves generated by natural hazard events. *Journal of Geophysical Research: Space Physics*, *120*, 8002–8024. https://doi.org/10.1002/2015JA021116

Zhang, S. D., & Yi, F. (2002). A numerical study of propagation characteristics of gravity wave packets propagating in a dissipative atmosphere. *Journal of Geophysical Research*, *107*, 4222. https://doi.org/10.1029/2001JD000864